UNIVERSIDAD DE VALLADOLID

ESCUELA DE INGENIERIAS INDUSTRIALES

Máster en Ingeniería Industrial

Iron-based catalysts for selective hydrogenation of 1,3-butadiene

Autor:

Santander de Soto, Laura

Responsable de Intercambio en la Uva:

Alfonso Redondo Castán

Sorbonne Université

Valladolid, Julio de 2018.

TFM REALIZADO EN PROGRAMA DE INTERCAMBIO

TÍTULO: **Iron-based catalysts for selective hydrogenation of 1,3-butadiene**

ALUMNO: **Laura Santander de Soto**

FECHA: **20 de Julio de 2018**

CENTRO: **Laboratory of Surface Reactivity**

TUTOR: **Laurent Delannoy**

ABSTRACT

Hoy en día, una gran mayoría de lo que nos rodea se ha fabricado a partir de polímeros obtenidos mediante la reacción de polimerización de pequeñas repetitivas subunidades (monómeros). Los monómeros más empleados en la industria son los alquenos ligeros. Sin embargo, su método de obtención da lugar a algunas impurezas (alquinos y alcadienos) que provocan la contaminación del catalizador. El objetivo de este estudio ha sido encontrar un catalizador adecuado para la hidrogenación selectiva del 1,3-butadieno ya que este proceso es una alternativa para conseguir purificar las corrientes de alquenos. Para ello, se han llevado a cabo dos métodos de preparación: "Chemical Reduction" y "Deposition-precipitation with urea". Además, distintas técnicas de caracterización tales como XRD, XRF, TEM-EDX, TPR, BET.. se han utilizado para conocer la estructura, composición y morfología de los materiales. Por último, los catalizadores basados en hierro fueron sometidos a análisis catalíticos en la reacción de hidrogenación selectiva de 1,3-butadieno con el fin de comprobar su actividad catalítica, selectividad y estabilidad. El material que presentó mejor comportamiento fue Fe-Zn $1:5/TiO_2$.

KEYWORDS

Iron-based catalysts for selective hydrogenation of 1,3-butadiene

Laura Santander de Soto

Master thesis submitted within an Erasmus programme +

Supervisor: Dr. Laurent Delannoy

Laboratory of Surface Reactivity

Chair: Prof. Dr. Hélène Pernot

Faculty of Chemistry

Academic year 2017-2018

Acknowledgements

Table of Contents

CHAPTER 1   INTRODUCTION

In the recent days, a high percent of all we are surrounded is made of polymers which are composed of many repeated subunits, i.e. the monomers. These monomers are used as raw materials in the catalytic polymerization reactions, in particular, light alkenes are employed as reagents for polymer synthesis in industry. However, steam reforming processes, which produce these monomers, lead to the formation of a few percent of alkadienes and/or alkynes as impurities which can easily poison the catalysts employed for polymerization reactions.

On the other hand, the selective hydrogenation has been the most applied method for decreasing the amount of dienes and alkynes contaminants. Supported metals catalysts are designed in order to avoid total hydrogenation of the main alkene stream. Therefore, the ideal catalyst for this reaction should be active (alkynes and dienes conversion), selective (no overhydrogenation) and stable.

Palladium has been the most used metal in the industry for gas and liquid-phase selective alkynes and/or alkadienes hydrogenation. It presents high activity but tends to absorb hydrogenation and could form hydrides leading to selectivity reduction. Iron is increasingly gaining interest owing to its low toxicity and its abundance on Earth. In fact, recently, iron has been the centre of renewed interest because of its ability to catalyse alkenes, carbonyls, imines or carbonates hydrogenation. Moreover, bimetallic nanoparticles reveal unique properties since they could exceed those of the separated metal components. Using DFT calculations, it has been demonstrated that Fe-Zn alloys can turn out being a promising system for the selective hydrogenation of polyunsaturated hydrocarbons.

Moreover, though some studies evinced no influence of the oxide support nature on the activity and selectivity during the selective hydrogenation indicating that the reaction only takes place on the metal particles, the requirements of the support are stability during sample preparation and no catalytic activity for selective hydrogenation. TiO_2-support is selected as the main one because of its stability in solution.

Two preparation methods, Deposition precipitation with urea and Chemical Reduction, are studied to synthesize the catalysts used for selective hydrogenation of 1,3-butadiene in the gas phase as a model reaction. The samples obtained by these two methods are characterized by several physico-chemical techniques, noticeably in order to estimate the degree of interaction between the two metals, Fe and Zn.

CHAPTER 2   LITERATURE SURVEY

The literature study mainly focusses on the purpose of alkene stream purification process through selective hydrogenation reaction. It discusses the use of supported mono- and bimetallic catalysts as well as different synthesis strategies. The selective hydrogenation of 1,3-butadiene as model reaction is the major focus.

2.1.   INTRODUCTION

2.1.1.   Main application

In the recent days, a high percent of all we are surrounded is made of polymers such as synthetic fabric, furniture, plastic containers, shell of most electronic products...[1] The term polymer derives from the ancient Greek words: *polus*, meaning `many,such´, and *meros* meaning `parts´ and refers to a large molecule whose structure is composed of many repeated subunits i.e., the monomers. These monomers are used as raw materials in the catalytic polymerization reactions leading to organic products known as polymers. Unsaturated hydrocarbons, and especially light alkenes like ethylene, propylene, but-1- and -2-enes, isobutenes, etc., are widely selected as reagents for polymer synthesis in industry [2],[3]. The demand of these raw alkenes in industry has increased exponentially. For instance, the requirement of propylene was only 47 million tons in 1998 and the value predicted for 2020 is around 160 million tons and, in the case of the largest basic chemical building blocks, ethylene, was only 80.5 million tons in 1998, approximately 175 in 2015 and for 2020 is above 200 million tons [4].

2.1.2.   Drawback and solution

The main production method of unsaturated hydrocarbons is cracking of petroleum hydrocarbons including heavy liquid fractions i.e., crude oil [5]. However, steam reforming processes take place at high temperature which results in the formation of a few percent of alkadienes and/or alkynes as impurities, i.e. 0.3 to 6.0% of residual butadiene in butenes, 0.5 to 3% of acetylene in ethylene and 2 to 8% of propyne and propadiene in propene [6], [7]. These impurities contained into the alkene cuts can easily poison the catalysts employed for polymerization reactions [2]. An example is illustrated by B.J.Burger et al. when 2-butyne impurity altercates the catalyst during 2-butene polymerization [8]. Thus, to avoid catalyst poisoning, impurity level must be controlled and not exceeded 10 ppm [9].

In essence, there are three alternatives to eliminate or reduce the alkynes and dienes impurities:

i.   Remove them by fractional distillation: uneconomic method, high energy consumption [10].

ii.   Extract them from alkene stream by solvent extraction or metal-organic frameworks (MOF) adsorption [10].

iii. Convert them into useful products by selective catalytic hydrogenation which is the focus of this report [10].

2.1.3.   Purpose

The selective hydrogenation is the most applied method for decreasing the amount of dienes and alkynes contaminants. Moreover, it is an important industrial process for the production of high purity alkene stream for further polymerization reactions [9]. In fact, the key issue of this purification process is to avoid total hydrogenation of the main alkene stream. For that purpose, supported metals catalysts are designed in order to achieve semi-hydrogenation of alkynes and dienes into alkenes without any oligomers and alkanes formation. Therefore, the ideal catalyst for this reaction should present high activity (satisfying low activation barrier for alkynes/dienes conversion), high selectivity (no overhydrogenation favouring limited alkanes generation) and high stability (avoiding oligomers formation through C-C coupling since they lead to catalyst deactivation by means of fouling) [11]. In addition, impurities conversion should be performed at a temperature as low as possible [2] and, from an industrial point of view, low price and easy preparation and regeneration also play a relevant role [12].

2.2.   RAW MATERIALS

2.2.1.   Iron based catalysts

Over the last years, palladium has been the most used metal in the industry for gas and liquid-phase selective alkynes and/or alkadienes hydrogenation because of its high activity which is, in turn, due to its low H_2 dissociation barrier [13]. Besides, it is selective when concentration of impurity is still high [5]. Nevertheless, Pd also has some disadvantages such as: its tendency to absorb hydrogen and form hydrides leading to selectivity reduction by formation of alkanes, and its trend to favour oligomerization and green oil formation on its surface diminishing catalytic stability [13]. As a result, for ultimate purification and elimination of alkadienes or alkynes traces, i.e., at high conversion, Pd catalysts are not selective enough. Furthermore, other drawbacks are its high metal cost, around 1000 dollars per kg [13] and the foreseen shortage of noble metals in the near future[14].

Therefore, it is convenient to look for new catalysts with an efficient behaviour in selective hydrogenation reactions and with abundant and cheap sources [13], [14]. In this respect, iron-based

catalysts are of a large interest owing to their low toxicity and the abundance of iron on Earth. Besides, taking also into account that nanometric-sized catalysts exhibit potential behaviour in catalysis due to the high ratio of surface atoms, iron-based NPs have been mostly used for different applications such as Fischer-Tropsch reaction, carbon nanotubes synthesis and biomedical applications [15]. Recently, iron has emerged at the centre of renewed interest in both homogeneous and heterogeneous hydrogenations. Iron-based materials can catalyse alkenes, carbonyls, imines or carbonates hydrogenation in addition to the selective hydrogenation of alkynes to alkenes which is, in fact, the purpose of this research [16]. For instance, an $Al_{13}Fe_4$ intermetallic compound showed high activity in butadiene partial hydrogenation with high selectivity to butenes at room temperature [14]. For that reason, it seems that iron nanoparticles can be a promising catalyst for selective hydrogenation of polyunsaturated hydrocarbons.

2.2.2. Bimetallic Fe nanoparticles

Bimetallic nanoparticles (NPs) are increasingly gaining importance owing to their unique properties. Depending on the respective future application such as catalysis, electrochemistry, magnetism, optics or biomedicine, structure properties of nanoalloys (e.g., shape, size, composition and surface chemistry) are different. In consequence, the diversity of NPs makes them extremely desirable. In the following scheme *(Figure 2.1)*, the main types of structure which are determined by the nature of elements i.e., relative bond strengths, surface energies, relative atomic sizes, charge transfer and specific electronic/magnetic effects, are represented [17].
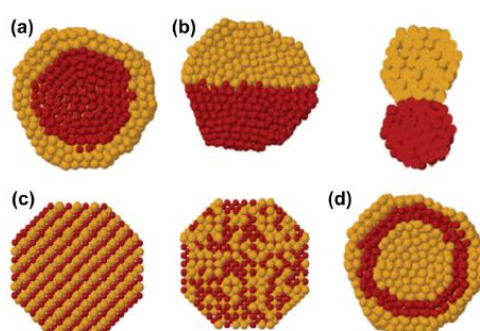
Figure 2.1. Schematic representation of bimetallic NPs with different structures. a) core-shell segregated structures; b) heterostructure; c) intermetallic or alloyed structures and d) multishell structures [17] .

In the area of catalysis, bimetallic catalysts are well known because their properties exceed those of the separated metal components as some experimental studies have showed using model surfaces [18]. For instance, average metal-metal bond length along with modifications of the electronic

structure due to orbital overlap changes are governing factors. However, improvements in activity and selectivity catalysts are the principle objective in this matter so special attention to geometric effect at the surface should be paid [18] since, for example, for bimetallic Pt/Ni system [19], the second metal (Ni) may block the first metal (Pt) sites on the surface and, then, average size and composition of active sites can be modified [18].

Concerning nano Fe which presents high reactivity, low cost, easily obtained raw materials and nontoxicity, as it has already been mentioned, catalytic performance of this metal in selective hydrogenation can be enhanced by combining with another non-noble metal [17]. No previous search has been carried out to explore the combination of Fe and Zn but some studies on other metals (Cu,Ni) have showed the promising effect of Zn addition on the catalytic performances[10]. In a study performed by F. Studt et al., DFT calculations predicted that Fe-Zn alloys could have interesting properties in terms of activity and selectivity for the acetylene hydrogenation reaction [20]. As a matter of fact, they went into detail to find the best catalyst for their purpose and, by means of Density functional theory (DFT), elaborated scaling relations between different adsorption energies of components in order to characterize their catalytic activity and selectivity. Through this DFT calculation, it can be predicted that bimetallic Fe-Zn or $FeZn_3$ alloys could be interesting alternatives for the selective hydrogenation of polyunsaturated hydrocarbons.

2.2.3. Support

Referring to the fact that solid catalysts are very functional materials employed in 90% of industrial processes, it is important to point out that the most important ones are supported. In these catalysts, nanoparticles of an active element (metal, oxide, or sulphide) are dispersed on the surface of a carrier with high surface area [21].

The requirements of the support for this study in particular are[10]:

- Stability during the sample preparation and the following thermal treatments.
- No catalytic activity for selective hydrogenation of unsaturated hydrocarbons.

To prepare very active and selective catalysts, it is of significance to have knowledge of morphology, structure and catalytic property of the solid used as a carrier in order to understand the relevant interfacial chemistry and fundamental deposition processes taking place at the interface developed between the carrier surface and the solution containing the precursor species of the active element to be deposited which is the most usual way to start a synthesis [21].

For this research, although some studies evinced that no influence of the oxide support nature on the activity and selectivity was found during selective hydrogenation of butadiene indicating that the reaction happens only on the metal particles [22], [23], conversely, P.Burattin et al.[24] and V.Kaushik et al.[25] reported that SiO_2 and Al_2O_3 supports can easily create silicates or aluminates species during sample preparation. For that reason, TiO_2 support has been selected because of its stability in solution and owing to the absence of reports about titanates formation during sample preparation at low temperature [21].

Titanium oxide is widely used in a lot of photocatalytic and classical catalytic processes due to the fact that it is chemically and biologically inert, stable to corrosion and nontoxic. It presents two important phases, anatase and rutile crystals, both are formed by chains of distorted TiO_6 octahedra where each Ti atom is surrounded by 6 oxygen atoms. Regarding tetragonal structure of anatase, the conventional unit cell contains four TiO_2 units, unlike that of rutile which consists of two TiO_2 units [21].

Regarding the selected metal, there are not a great deal of studies on the deposition of Fe(II) on TiO_2 in the literature, probably, since Fe(II) is very easily oxidised to Fe(III) so it is hard to find convenient conditions to work under. However, some authors have studied kinetics and equilibrium of the adsorption of Fe(II) on TiO_2 oxide rich in anatase (P25) which it is well known to develop hydroxyl groups on the surface as it occurs when the surface of an oxide is in contact with an electrolyte solution[21], [26]. Then, in order to fit properly the data of adsorption using the most realistic model (multisite complexation model or music), Hiemstra and Van Riemsdijk assumed that this deposition gives rise to the formation of a tetradentate inner-sphere complex *(Eq. 1)* [27].

$$2\,Ti_2O^{-0.67} + 2TiOH^{-0.33} + Fe^{2+} \leftrightarrow (Ti_2O)_2(TiOH)_2Fe \qquad \textit{Eq. 1} \;[27]$$
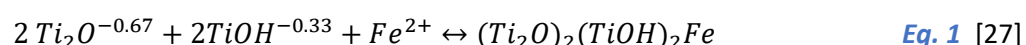
2.3. SYNTHESIS STRATEGY

Numerous methods of synthesizing bimetallic NPs have been reported for the last decades. They can be generated in solution, in gas phase, in a matrix or supported on a substrate. In summary, method can be classified into two main types: physical methods such as radiolysis, mechanical alloying method, impregnation in excess of solution or anionic adsorption; and chemical methods like electrochemical method, chemical reduction, thermal decomposition or deposition-precipitation [17], [23].

Recent research has showed that the preparation method has a strong influence on the activity towards hydrogenation reaction. In fact, it was found that catalysts prepared by deposition-precipitation presented higher activity. For that reason, this synthesis method has been chosen for further investigation [23].

On the other hand, chemical reduction has resulted in being an interesting method to prepare nanoscale zero-valent iron in order to be used in environmental applications because of its reactivity toward targeted contaminants [28], [29]. Due to the fact that it has also been tested as catalyst in some hydrogenation processes [30], [31], it is another synthesis choice in this particular study.

2.3.1.   Deposition-precipitation with urea (DPu)

The first who proposed deposition-precipitation by a gradual and continuous increase of the pH to synthesise supported metal catalysts was Geus et al. for the preparation of Ni/SiO_2 who pointed out that the phase diagram of the precipitated solid in equilibrium with a solution containing its metal precursor as a function of temperature and concentration of a precipitation reactant (e.g. sodium hydroxide, ammonia and urea) must be taken into account. The equilibrium curves represented by solubility (S) and supersolubility (SS) curves, whose intermediate gap corresponds to the nucleation, of a pure solution and a solution with a support in suspension can be observed in *(Figure 2.2)* [32].

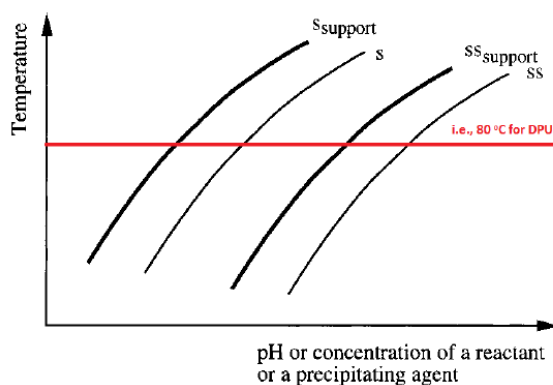**Figure 2.2.** Phase diagram as a function of temperature and concentration of a reactant for a pure solution (solid lines) and a supported solution (bold lines) [32]

Noting that, in the case of supported materials like the catalysts in this study, to favour the metal precipitation on the support and avoid it in solution, the pH must be controlled between the concentration of the two supersolubility curves [32].

On the other hand, as this method is performed in isothermal condition, specifically at 80 °C for DPu *(Figure 2.2)*, the concentration of soluble ions will diminish little by little owing to deposition-precipitation onto support surface, in other words, during pH increase *(Figure 2.3)*. This is due to the gradual rise of precipitating agent (OH⁻) which leads to precipitation by hydrolysis of the metal complexes promoting a fluctuation in OH⁻ concentration.
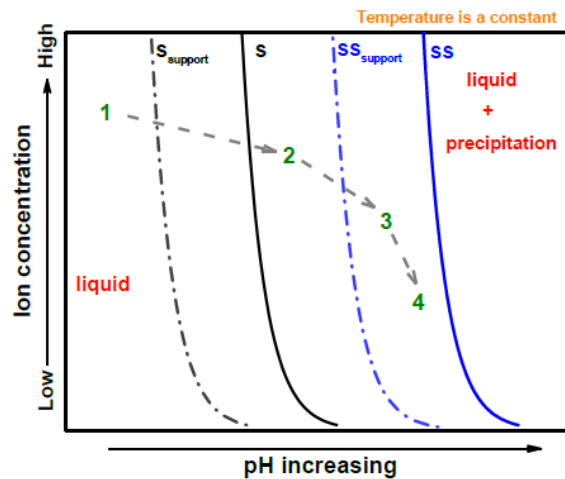
Figure 2.3. Phase diagram of precipitation of metal species in solution as a function of pH and ion concentration: a pure solution (solid lines) and a supported solution (dotted lines) [10]

It is also of significance for bimetallic materials synthesis to consider that if it is desired that the two metal ions are co-deposited on the support in a single step, solubility products must be closed to each other. In *Table 2.1*, the values of solubility products of some base metal hydroxides at room temperature are described [33]:

$M(OH)n$	$K_{sp}^{\ominus} M(OH)_n$
$Zn(OH)_2$	4.1×10^{-17}
$Cu(OH)_2$	2.0×10^{-19}
$Ni(OH)_2$	5.5×10^{-16}
$Fe(OH)_2$	4.9×10^{-17}
$Fe(OH)_3$	6.0×10^{-38}

Table 2.1. Solubility products of non-noble metal hydroxide at RT [10], [33]

Therefore, it is supposed that the selected metals, i.e., Fe and Zn, will be deposited onto the support at the same time during pH increase according to their similar solubility products (Fe^{2+} and Zn^{2+}).

Urea has been selected as the precipitating agent to synthesise these particular catalysts because of being a delay-base, i.e., its dissolution and decomposition during solution basification can happen into two separated steps controlled by the solution temperature. This statement means that urea is capable of dissolving into solution at RT and then decomposing to CO_2, NH_4^+ and OH^- above 60 °C *(Eq. 2)* [12], [30].

$$CO(NH_2)_2 + 2H_2O \rightarrow CO_2 + 2NH_4^+ + 2OH^- \hspace{2cm} \textit{Eq. 2}$$
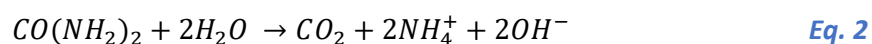
2.3.2. Chemical reduction

Nowadays, one of the most common method of synthesizing metallic NPs because of its simplicity is chemical reduction of metal salts in a solution using proper reducing agents such as $NaBH_4$, H_2, NH_2-NH_2... In this case, sodium borohydride ($NaBH_4$) has been selected as reducing agent since Fe precursors are difficult to reduce because of its low redox potential [17].

$$Fe(H_2O)_6^{2+} + 2\,BH_4^- \rightarrow Fe^0 \downarrow + 2B(OH)_3 + 7\,H_2 \hspace{2cm} \textit{Eq. 3}$$
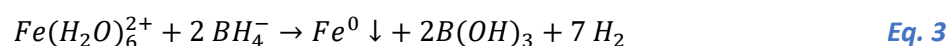
This process is referred in the literature as bottom up [28] since it is based on the production of nanoscale zero-valent iron (nZVI) which is an engineered nanomaterial widely used in environmental remediation and hazardous waste treatment [31].
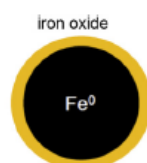
Figure 2.4. Structure of fresh nZVI

nZVI displays high reactivity due to its classical core-shell structure which consists of a metallic iron (Fe(0)) core encapsulated by a thin iron oxide shell of a few nanometers. In a way that the oxide shell promotes the adsorption of contaminants via electrostatic interactions and surface complexation, whereas Fe(0) works as an electron source applies a reducing character [29], [31].

However, nZVI also presents some weaknesses including a lack of stability, rapid passivation of the material and limited mobility of the particles due to the formation of agglomerates. Therefore, nZVI are being frequently modified in order to increase its effectiveness and because it performs well in the role of a modifier [28]. For instance, it can be employed as a material enhancing the work of a catalyst

based on TiO_2 achieving more efficiency and 'life span' increase [35]. For this reason, among all the alternatives of nZVI modification such as doping with other metals, surface coating, emulsified nZVI or deposition on a support, the latter has been chosen to synthesise the nanoparticles in the current study. Apart from TiO_2, SiO_2 support also resulted in beneficial effects because it achieved to reduce the aggregation with simultaneous preservation of high nZVI activity as Li et al. reported [36].

Thus, for these reasons, TiO_2 and SiO_2 were used as support to prepare nZVI by Chemical reduction.

2.4. SELECTIVE HYDROGENATION OF 1,3-BUTADIENE

This study is focused on catalytic behaviour of synthesised catalysts in hydrogenation of 1,3-butadiene. Among all the model reactions of selective hydrogenation of alkynes and alkadienes in alkenes, this particular reaction has been chosen because it gives four different products (three butenes and butane), with 1-butene as the most desirable product, and therefore allows the study of both activity and selectivity issues [23].

First of all, it is known that the molecule of 1,3-butadiene presents two distinct configurations: trans-1,3-butadiene and cis-1,3-butadiene *(Figure 2.5)*. Both exhibit the same values for C-H, C-C and C=C bond lengths, 0.108, 0.148 and 0.137 nm respectively. In addition, there is a super π bond due to the orbital overlapping of 2p-2p in C atoms which joins the four carbon atoms in butadiene molecule.
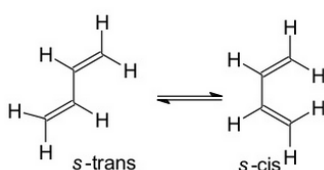

Figure 2.5. Molecular conformation of A) Trans-1,3-butadiene and B) Cis-1,3-butadiene [10] .

2.4.1. Hydrogenation of 1,3-butadiene

Three possible routes to hydrogenate 1,3-butadiene are found: $1,2-H_2$ addition, $1,4-H_2$ addition and $2,3-H_2$ addition *(Figure 2.5)*.
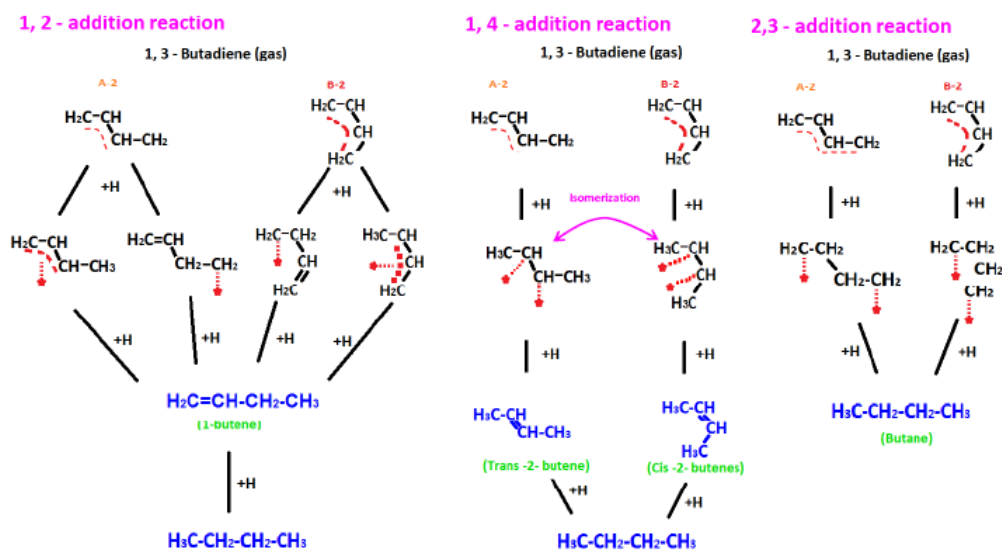
Figure 2.6. Scheme of three different hydrogen addition reaction on 1,3-butadiene [10] .

As far as it is observed in the representation *(Figure 2.6)*, 1,2-addition gives place to 1-butene formation by means of two hydrogen atoms addition onto C1 and C2 atoms. Similarly, for 1,4-addition, two hydrogen atoms are added onto C1 and C4 atoms resulting in cis-2-butene and/or trans-2-butene generation. In these both cases, hydrogenation could continue and lead to butane. Nonetheless, during 2,3-addition, butadiene is totally hydrogenated to butane due to the fact that an unstable intermediate product is generated ($*CH_2CH_2CH_2CH_2*$) which rapidly reacts with other two H atoms and forms the butane product [10]. On the other hand, another alternative reaction has been reported by Gómez et al. [18], it is isomerization which can transform trans-2-butene into cis-2-butene.

As it has already been mentioned, a lot of steps take place during a chemical reaction of petrochemical interest and some of them lead to undesired products by the so-called side reactions. That it is the reason why alkenes conversion by transition metals is one of the most studied catalytic reactions, mainly, because some relevant issues are still unresolved. In particular, selective hydrogenation of 1,3-butadiene, which is an impurity in butenes stream produced from oil cracking with concentration 0.3 to 6% [6], is considered as a reaction test for probing electronic structure and activity of metal catalysts [18]. The purpose is to generate only butenes and to prevent butane formation. Therefore, 2,3-addition must be avoided and 1,2- and 1,4-additions are supposed to arise on the catalyst surface without any further hydrogenation reactions [10].

2.4.2. Selective hydrogenation of 1,3-butadiene in the excess of propene

In this work, selective phase hydrogenation of 1,3-butadiene performed in an excess of propene (propene/butadiene ratio = 100 ; 0.3% butadiene, 30% propene and 20% hydrogen) has been selected in order to simulate the purification process of industrial light alkenes stream (C4 cuts) to prevent further poisoning of the polymerization catalysts used for polyalkene production [37].

The choice of replacing butene by propene was based on the experimental results of previous research which demonstrated that the reactivity of propene was similar to that of butenes [23], [37]. In fact, despite the assumed fact that adsorbed propene limits the access of catalytic sites to the other reactants, these studies probed that propene must be weakly adsorbed, otherwise butadiene hydrogenation would be inhibited. Thus, alkene adsorption on the catalytic sites is not a parameter limiting the reaction rate [37].

In conclusion, with the purpose of an easy distinction by gas chromatography between alkane (butane) arising from the total hydrogenation of 1,3-butadiene and that (propane) arising from hydrogenation of the alkene in excess, propene is selected as the main alkene rather than butene [23].

As a summary, 1,3-butadiene is expected to be semi-hydrogenated to butenes (1-butene, trans-2-butene or cis-2-butene) with no further butane formation and no propane generation derived from propene hydrogenation [10].
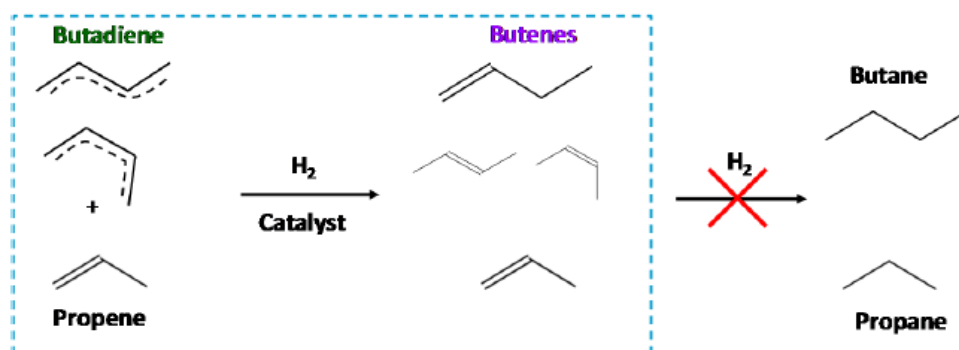

Figure 2.7. Selective hydrogenation in the gas mixture [10] .

CHAPTER 3   MATERIALS AND METHODS

The aim of this chapter is to describe the procedures followed towards the synthesis, characterization and testing of catalysts selected for selective hydrogenation reaction.

3.1. MATERIAL SYNTHESIS

3.1.1. Deposition-precipitation with urea (DPu)

Monometallic Fe/TiO_2 and Zn/TiO_2 and bimetallic $Fe-Zn/TiO_2$ catalysts were prepared using the method of deposition-precipitation with urea (DPu) described in Section 2.3.1. For this procedure, 3 g of support (TiO_2 P25 Evonik, 80 % anatase, 20 % rutile) were weighed and dispersed into 300 ml of distilled water ($m_{support(g)} : V_{water(ml)} = 1:100$) previously heated at 80°C using a water bath and which contains, the stoichiometric amount of metal precursor(s) such as $FeCl_2 \cdot 4H_2O$ and $ZnCl_2$ in order to achieve the desired nominal metal loading, i.e., 2.5 wt% Fe with Fe:Zn atomic ratios of 1:1 and 1:5. Once the support was added into the mixture, the precipitating agent (urea) must be immediately introduced in excess with a molar concentration ratio of [urea]/[metal] = 100. The mixture was kept at 80 °C in a closed double-wall reactor for 16 h under continuous stirring. After that, the precipitated solid was separated from the liquid phase by centrifugation and subsequently repeatedly washed with distilled water and centrifuged (three times). At last, samples were dried under vacuum at room temperature for 24 h and, once they were crushed, sieved and weighed, activation through thermal treatment was performed (see Section 3.2.).

All chemicals were supplied by Sigma Aldrich. Metal precursors were: $FeCl_2 \cdot 4H_2O$ (198.81 g/mol), $ZnCl_2$ (136.28 g/mol); Support: TiO_2 P25 Evonik (79.87 g/mol) and precipitating agent: $CO(NH_2)_2$ (60.06 g/mol).

3.1.2. Chemical reduction

Zero-valent iron (ZVI) were synthesised by the Chemical Reduction method described in Section 2.3.2. Different procedure conditions were attempted such as distinct inert gases and several main solution chemicals. Finally, it was found that working under Argon degassing using Milli-Q water (18.2 MΩ·cm at 25 °C) as solvent were the best conditions for this synthesis method.

Before starting the preparation, high purity water was subjected to degassing by Ar for 30 minutes. Next, 85 mL were separated and put in a round-bottom flask under stirring at room temperature without stopping Ar degassing. Then, the appropriate amount of iron precursor was weighed and added to the solution. The pH was measured (≈3.4) after dissolution and continuous stirring for 5 min. Then, 1 g of support (TiO_2, SiO_2 or Zn/TiO_2) was introduced into the solution and stirring was kept for

10 additional minutes while a fresh NaBH$_4$ solution (0.44 M) was prepared. The latter consisted of 83 mg of solid precursor NaBH$_4$ dissolved in 5 mL of degassed Milli-Q water. At the same time that NaBH$_4$ was added dropwise, the iron solution colour was changing from light pink to light brown, light grey and, then, dark grey for Fe/TiO$_2$ whereas, in the case of Fe/SiO$_2$, material turned very dark grey just after the moment of addition. After keeping on stirring for 10 min, the precipitated solid was separated from the liquid phase by centrifugation and subsequently repeatedly washed with Milli-Q water and centrifuged (two times). Finally, samples were dried under vacuum at room temperature for 24 h and, once they were crushed, sieved and weighed, activation through reduction treatment was performed (see Section 3.2.).

All chemicals were also supplied by Sigma Aldrich. Metal precursors were: FeCl$_2$·4H$_2$O (198.81 g/mol), ZnCl$_2$ (136.28 g/mol); Support: TiO$_2$ P25 Evonik (79.87 g/mol), SiO$_2$ (60.08g/mol) and reducing agent: NaBH$_4$ (g/mol).

3.2. THERMAL TREATMENT

After the procedure described in section 3.1., a thermal treatment was performed on the samples before characterization and catalytic tests. The materials prepared by DPu were subjected to a calcination treatment for 2 h at 400°C with a temperature ramp of 5°C min^{-1} under flowing air ('x' mL min^{-1} for 'x' mg of sample) and, then, to a reduction process at both 400 and 500 °C for 2 h with a temperature ramp of 3°C min^{-1} under flowing H$_2$ ('x' mL min^{-1} for 'x' mg of sample). In the case of the samples synthesised by Chemical Reduction, the reduction treatment is directly performed without previous calcination since iron was already reduced and Fe reoxidation should be avoided as much as possible.
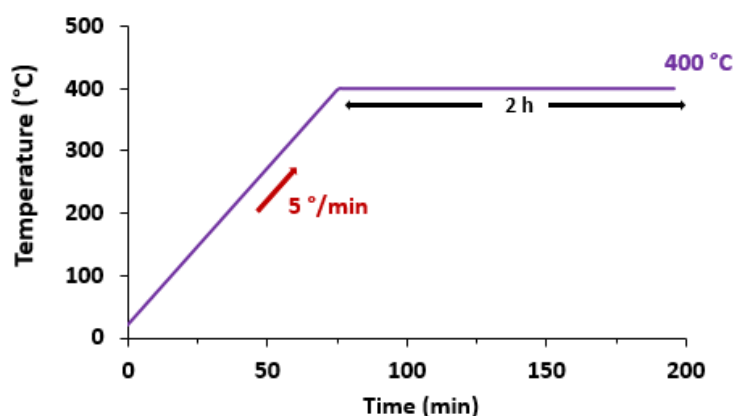

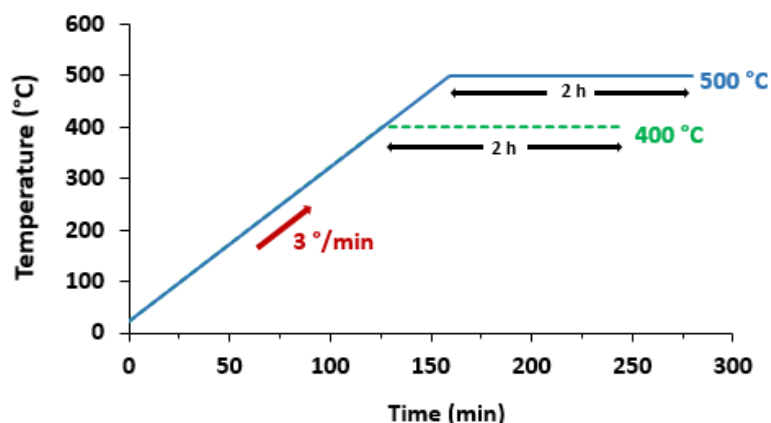*Figure 3.1.* Temperature program for calcination.

Figure 3.2. Temperature program for reduction.

3.3. MATERIAL CHARACTERIZATION TECHNIQUES

The following experimental setups were used to characterize the samples and to analyse their physico-chemical properties.

- **XRF:** XEPOS HE (AMETEK).
- **XRD:** D8 Bruker Company.
- **N_2- adsorption**: BELSORP-max.
- **TEM, STEM-HAADF, EDX**: JEOL 2100Plus, CCD Orius camera Gatan, Oxford, SDD 80 mm^2 Xmax.
- **TPR**: Varian Micro GC QUAD CP4900.

3.3.1. X-Ray Diffraction (XRD) analysis

The measurement was performed on a diffractometer (D8 Bruker Company) operating with Cu Kα radiation (1.5418 Å; 40 kV and 30 mA) with a Ni filter and XRD peaks were detected with the JCPDS cards.

Crystallite size can be estimated by Scherrer's equation calculation using full-width half maximum (FWHM) of each characteristic peak.

$$\bar{d} = \frac{K\,\lambda}{\beta\,\cos\theta}$$

Eq. 4

Where λ is the wavelength of the X-ray (0.15406 nm); *d* is the average particle size (diameter in nm) ; K is a dimensionless shape factor with a value close to 0.89, θ is the Bragg angle in ° and, finally, β is the full width at half the maximum intensity (FWHM) with rad unit (1° = π/180 rad). Both Bragg angle and FWHM are obtained through XRD patterns using EVA software.

3.3.2. X-ray fluorescence (XRF) analysis.

It is also a non-destructive analytical technique used to determine the elemental composition of materials. XRF is based on the emission of the fluorescent (or secondary) X-ray from a sample which has been previously excited by bombarding with a primary X-ray source such as high energy X-rays or gamma rays which were firstly applied by Glocker and Schreiber et al. [38]. It is an excellent technology for qualitative and quantitative analysis of material composition, or in this case of metal loading, because each one of the elements produces a set of characteristic fluorescent X-rays that is unique for that specific element. Therefore, this method is based on calibration curves obtained from standard samples for each element. The measurements in the laboratory are carried out using a spectrometer XEPOS HE (AMETEK) [10].

3.3.3. N_2-adsorption analysis. Brunauer–Emmett–Teller (BET).

Before carrying out the experiment, samples must be pre-treated in order to remove all the other gases in the sample such as H_2O or CO_2 since the aim is to measure properties using N_2 adsorption. Hence, once samples are weighed, they were heated at 300 °C for 2h on a Belprep II.
Brunauer-Emmet-Teller surface area was determined by N_2-physisorption using a BELSORP-max designed for wide range adsorption isotherm for surface area and pore size distribution analysis. It can measure from relative pressures as low as $1x10^{-8}$ (N_2 at 77K, Ar at 87K).

3.3.4. Transmission Electron Microscopy (TEM)

The morphology of the metallic nanoparticles was observed by Transmission Electron Microscopy (TEM) on a JEOL 2100Plus, operated at 200 kV and equipped with a LaB6 gun. To better distinguish metal particles from the support, scanning transmission electron microscopy in high-angle annular dark-field mode (STEM-HAADF) were also performed to study small mono and bimetallic particles. The image was obtained by a CCD Orius camera Gatan. Energy-dispersive X-ray spectroscopy (EDX) characterization was carried out using Oxford, SDD 80 mm^2 Xmax with Aztec as software in order to evaluate the composition of metal particles.
Specimens were prepared by immersion of a lacey carbon film on a copper support grid into the as prepared sample by blowing off the excess of powder.

3.3.5. Temperature-Programmed Reduction (TPR)

With the purpose of testing the reduction behaviour of materials, the samples were kept under He flow at 100°C for 15h and were then exposed to a hydrogen flow of 100 ml min^{-1} at increasing temperature from 100°C to 400°C or 500°C with a rate of 2°C/min. The software used for collecting the data calculate the concentration of H_2O which is being formed through the experiment. In this way, comparing the value obtained experimentally with the theoretical amount of H_2O that the material should produce knowing its composition and the products of reaction, it is possible to estimate the extent of the reduction of the synthesised material and also to know approximately its temperature of reduction.

This analyses were undertaken by a Varian Micro GC QUAD CP4900 equipped with two analysis channels (Poraplot Q for H_2O detection).

3.4. CATALYTIC TEST AND PERFORMANCE

The performance of synthesised catalysts in selective butadiene hydrogenation was tested on 50 mg of sample (sieve fraction, 125-200 μm) in a plug flow microreactor in Pyrex (4 mm of internal diameter) *(Figure 3.3)*. Firstly, the *ex situ* calcined catalysts were activated *in situ*, under pure H_2 (100 mL min^{-1}) from RT to 400°C at a heating rate of 3°C min^{-1} and kept 2 h at the final temperature. Then, the reactor was cooled down were cooled down to room temperature under the same flow rate of pure H_2, and the reaction mixture containing 0.3% butadiene, 30% propene and 20% hydrogen in He (49.7%) with a total flow rate of 50 mL min^{-1} was first analysed as a reference by means of a gas chromatograph (Perichrom PR 2100, FID detector with a 7.5 m column (1/8 in.) filled with sebaconitrile 25% Chromosorb PAW (80/100 Mesh). After that, the reaction gas mixture was introduced in the reactor at RT and the outlet gas, i.e., reactants and products, was analysed by gas chromatography. The Winilab 4.0 software was used for data acquisition and extraction of the concentrations of the different gases detected. The catalytic study consisted of two or three analysis at RT. Then, gas analysis was performed every 15 min, i.e., every 30°C, between 30 and 200 °C (heating rate of 2°C/min) and when this temperature was reached, the reaction was continued for approximately 20h at 200°C.

The increase in temperature of the reactor in an oven was controlled via temperature program and the composition of gas mixture was controlled by mass flow controllers with a concentration ratio between butadiene and propene of 1:100.
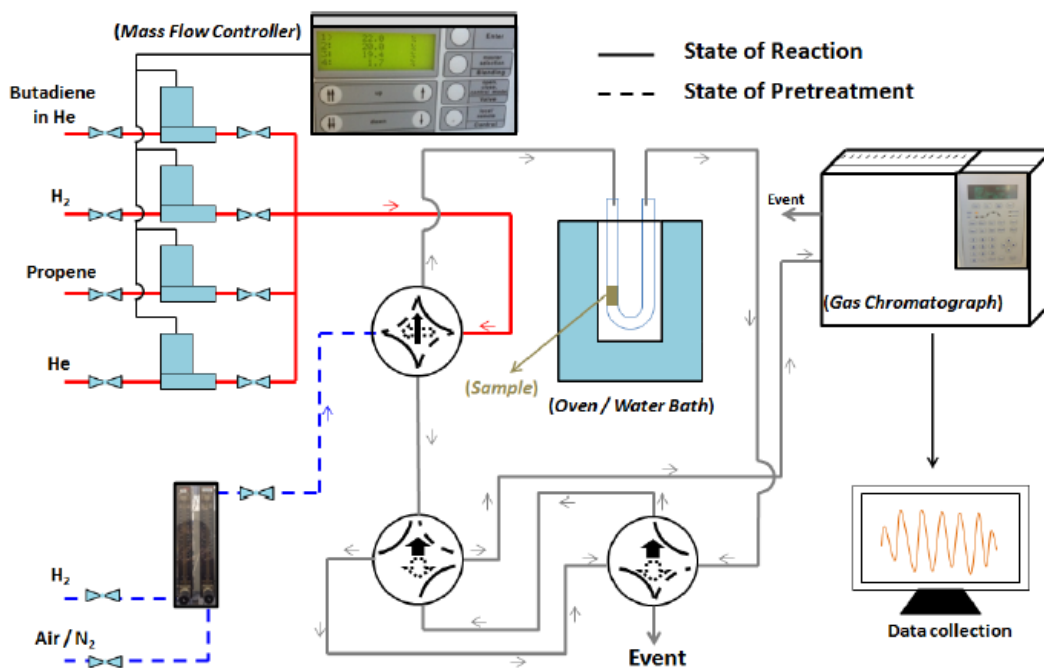

Figure 3.3. Scheme of catalytic test set-up

o   EVALUATION OF CATALYTIC PERFORMANCE

Catalytic properties of the samples are evaluated as follows:

a. *The selectivity*:

$$Alkanes\ formation\ (ppm) = (propane_{outlet} - propane_{inlet}) + butane$$

b. *The activity*:

$$Conversion_{butadiene}(\%) = 100\ x\ (1 - \frac{Butadiene_{outlet}}{Butadiene_{inlet}})$$

CHAPTER 4   RESULTS

4.1.   CHARACTERIZATION

In this section a structural investigation on the as-prepared and activated Fe-based catalysts has been performed using X-Ray Fluorescence (XRF), X-Ray Diffraction (XRD) and Transmission Electronic Microscopy (TEM). In addition, the reduction behaviour of these materials were investigated by monitoring the formation of H_2O during a reductive thermal treatment under H_2.

4.1.1.   X-ray fluorescence (XRF)

Based on the calculation and Fe metal loading selected for the synthesis of the samples, i.e., 2.5 wt%, the mass percent of Zn in the case of the bimetallic catalysts should be 2.78 wt% or 12.5 wt%, respectively, depending on the Fe-Zn molar ratio, 1:1 or 1:5. All theoretical mass percent, either for samples prepared by DPu or those by Chemical Reduction, have been included in *Table 4.1*.

THEORETICAL PERCENT OF MASS

	Fe samples	Fe-Zn 1:1 sample	Fe-Zn 1:5 samples
wt% Fe	2.5	2.5	2.5
wt% Zn	-	2.78	12.5
wt% TiO_2	97.5	94.72	85
wt% SiO_2	97.5	-	-

Table 4.1. Theoretical mass percent of each compound

In order to verify these theoretical mass, X-Ray Fluorescence (XRF) analyses were carried out for the as-prepared samples as well as for the samples after activation treatments, i.e., calcination and reduction processes. The results are summarised in *Table 4.2* for samples synthesised by Deposition-precipitation and in *Table 4.3*, for samples by Chemical Reduction.

EXPERIMENTAL MASS PERCENT OF SAMPLES BY DPU

	Fe	Zn	TiO_2
Fe/TiO_2	2.46	-	95.2
calcined Fe/TiO_2	2.55	-	93.7
500˚C-reduced Fe/TiO_2	2.55	-	94.9
400˚C-reduced Fe/TiO_2	2.39	-	95.1
Fe-Zn 1:1/TiO_2	2.46	2.65	92.6
calcined Fe-Zn 1:1/TiO_2	2.40	2.62	92

500˚C-reduced Fe-Zn 1:1/TiO₂	2.44	0.68	94.7
400˚C-reduced Fe-Zn 1:1/TiO₂	2.33	2.44	93
Fe-Zn 1:5/TiO₂	2.21	11.12	82.7
calcined Fe-Zn 1:5/TiO₂	2.19	10.80	83.4
500˚C-reduced Fe-Zn 1:5/TiO₂	2.17	9.30	84.9
400˚C-reduced Fe-Zn 1:5/TiO₂	2.19	10.88	83.1
Zn/TiO₂	-	12.30	83.4
calcined Zn/TiO₂	-	11.01	85.5
400˚C-reduced Zn/TiO₂	-	11.53	81.7

Table 4.2. *XRF analyses of Fe, Zn and TiO2 loadings in the samples prepared by DPu*

By and large, it can be affirmed that Fe and TiO$_2$ mass percent achieved are very similar to those expected. Therefore, it is concluded that Fe has been well deposited on TiO$_2$ surface. The zinc loadings are lower than the theoretical values, indicating an incomplete deposition of Zn. Moreover, in the same way that T.Imoto et al. and S.Lew et al. reported [39], [40] , the volatility of metallic Zn has been demonstrated by means of these XRF analyses undertaken in the samples reduced at 500 °C. As far as it can be appreciated in *Table 4.2*, the content of Zn has largely decreased after the reduction at 500 °C, especially in the sample with a molar ratio Fe-Zn of 1:1, comparing the Zn loading of 0.68 wt% obtained experimentally to the theoretical value, 2.78 wt%. Reduction at lower temperature (400 °C) allows to strongly limit such a loss of Zn, whatever the zinc loading.

On the other hand, the results show that Fe deposition on the TiO$_2$ surface was more incomplete using the Chemical Reduction method *(Table 4.3)* since the iron content tested by XRF was less than that obtained by DPu. Nevertheless, for the bimetallic sample which was prepared by combining both methods, i.e., firstly DPu process to synthesise Zn/TiO$_2$ and then, Fe addition by Chemical Reduction, XRF analysis shows that Fe was well deposited as well as no loss of Zn after reduction at 400°C was detected. Lastly, as the SiO$_2$ support is an amorphous material with higher surface area than TiO$_2$, it was not surprising that a higher Fe loading was achieved on its surface.

EXPERIMENTAL MASS PERCENT OF SAMPLES BY CHEMICAL REDUCTION

	Fe	Zn	TiO₂	SiO₂
Fe/TiO₂	2.15	-	95.68	-
400˚C-reduced Fe/TiO₂	2.14	-	95.74	-
Fe/SiO₂	2.96	-	-	91.94
400˚C-reduced Fe/SiO₂	3.14	-	-	94.19

Fe-Zn 1:5/TiO$_2$	2.69	11.77	79.92	-
400˚C-reduced Fe-Zn 1:5/TiO$_2$	2.92	12.56	79.91	-

Table 4.3. XRF analyses of Fe, Zn and support loadings in the samples prepared by Chemical reduction

Additional experiments using N$_2$-physisorption were performed so as to test the surface area (by BET method) of the supports as well as the state of some samples after metal addition. Results are tabulated in *(Table 4.4)*.

	BET surface area (m^2/g)
TiO$_2$ support	58.53
SiO$_2$ support	255.73
Fe/TiO$_2$ Chem Red	60.13
Fe/SiO$_2$ Chem Red	282.01
Fe/TiO$_2$ DPu	56.28
Zn/TiO$_2$ DPu	62.65

Table 4.4. BET surface area by N$_2$-physisorption

4.1.2. Temperature Programmed Reduction (TPR)

After observing the Zn loss at 500°C by XRF analysis, it was considered to probe the reduction behaviour of the Fe nanomaterials at 400°C and/or 500°C. The experiments were based on the comparison between the theoretical amount of H$_2$0 that should be produced during the reduction calculated by some estimations and assumptions and the experimental amount of H$_2$0 produced under a H$_2$ flow over the increase in temperature. Despite the fact that samples were initially calcined *ex-situ* at 400 °C for 2 h and, then, kept under a flow of He at 100 °C overnight before the TPR experiments, the amount of H$_2$O generated at low temperature, i.e., from 100 °C up to 250°C, is probably "structural" water removed from the bulk material and does not correspond to the reduction process. On the other hand, from 250°C, the formation of H$_2$O is considered to be due to the reduction of the material. In particular, Fe reduction consists in the following steps: Fe$_2$O$_3$ to Fe$_3$O$_4$ to FeO and, finally, to metallic Fe [41]. The total amount of water released has been estimated by calculating the area under the curve using the trapezoidal rule and was compared to the theoretical H$_2$O formation expected from the full reduction of Fe$_2$O$_3$ to Fe *(Table 4.5)*.

THEORETICAL AND EXPERIMENTAL H₂O FORMATION

	Theoretical H_2O production (mole)	Experimental H_2O production (mole)	*Ratio* Experimental/Theoretical
Fe/TiO₂ DPu reduction 500°C	$6.83 \cdot 10^{-5}$	$7.07 \cdot 10^{-5}$	1.03
Fe/TiO₂ DPu reduction 400°C	$6.40 \cdot 10^{-5}$	$4.82 \cdot 10^{-5}$	0.75
FeZn 1:1/TiO₂ DPu reduction 500°C	$5.86 \cdot 10^{-5}$	$7.80 \cdot 10^{-5}$	1.33
FeZn 1:5/TiO₂ DPu reduction 400°C	$5.86 \cdot 10^{-5}$	$6.48 \cdot 10^{-5}$	1.10
Fe/TiO₂ CR reduction 500°C	$5.75 \cdot 10^{-5}$	$4.77 \cdot 10^{-5}$	0.83
Fe/SiO₂ CR reduction 500°C	$7.92 \cdot 10^{-5}$	$8.70 \cdot 10^{-5}$	1.09

Table 4.5. Theoretical and experimental H_2O formation during the reduction under H_2

The reduction up to 400°C and 500°C of the Fe/TiO₂ sample prepared by DPu are represented in *(Figure 4.1)*. At first sight, it is supposed that Fe-based materials are more completely reduced at 500 °C but it is also worth to test their behaviour at 400 °C because of the important benefits for bimetallic FeZn-catalysts. Our estimations showed that Fe/TiO₂ reduced up to 500 °C is able to produce approximately the same amount of water as that of in the theoretical case *(Table 4.5)* but, when the reduction is stopped at 400 °C, it appears that the reduction is not complete.
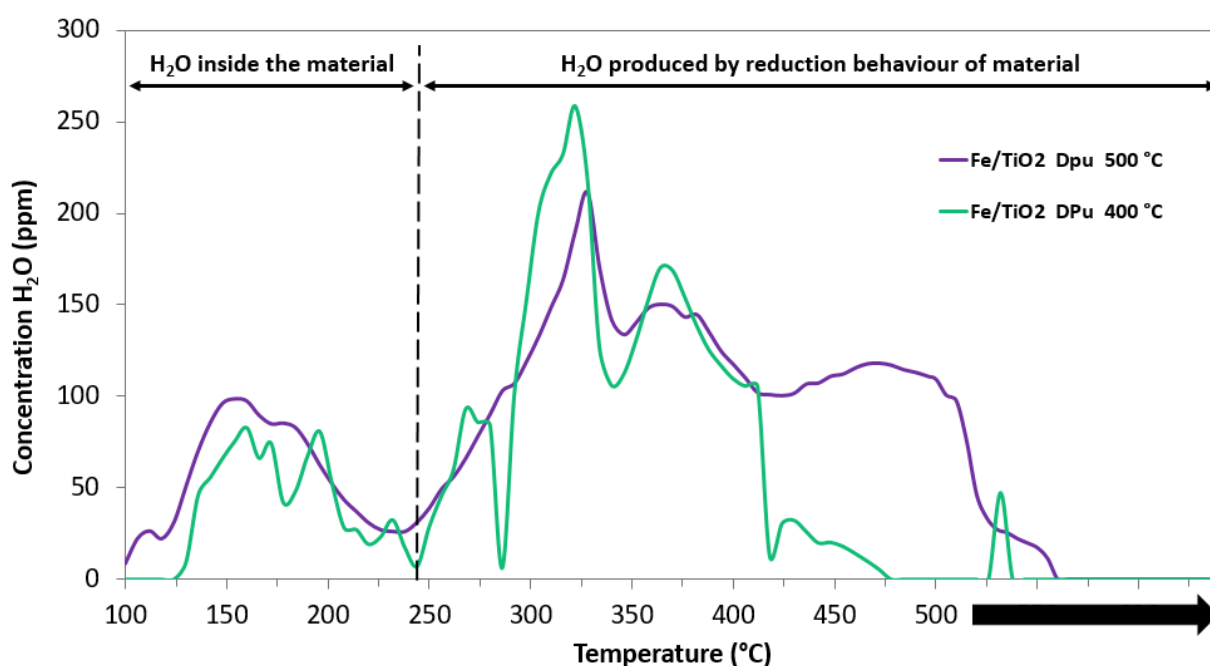
Concerning the Fe/TiO$_2$ and Fe/SiO$_2$ samples synthesised by Chemical Reduction, the amount of H$_2$O releases below 250°C is larger because these samples were not subjected to calcination before reduction. Additionally, as it was expected from XRF results, the higher water formation for Fe/SiO$_2$ is due to the more elevated content of iron. In the case of Fe/TiO$_2$, the water formation is also clearly lower than for the same sample prepared by DPu *(Figure 4.2)*. This may result from the fact that for the samples prepared by Chemical Reduction, iron was already reduced by reaction with NaBH$_4$ during the preparation and was then reoxidised by exposure to air, but the extent of the reoxidation is unknown, as is the nature of the iron oxide phase(s) formed.
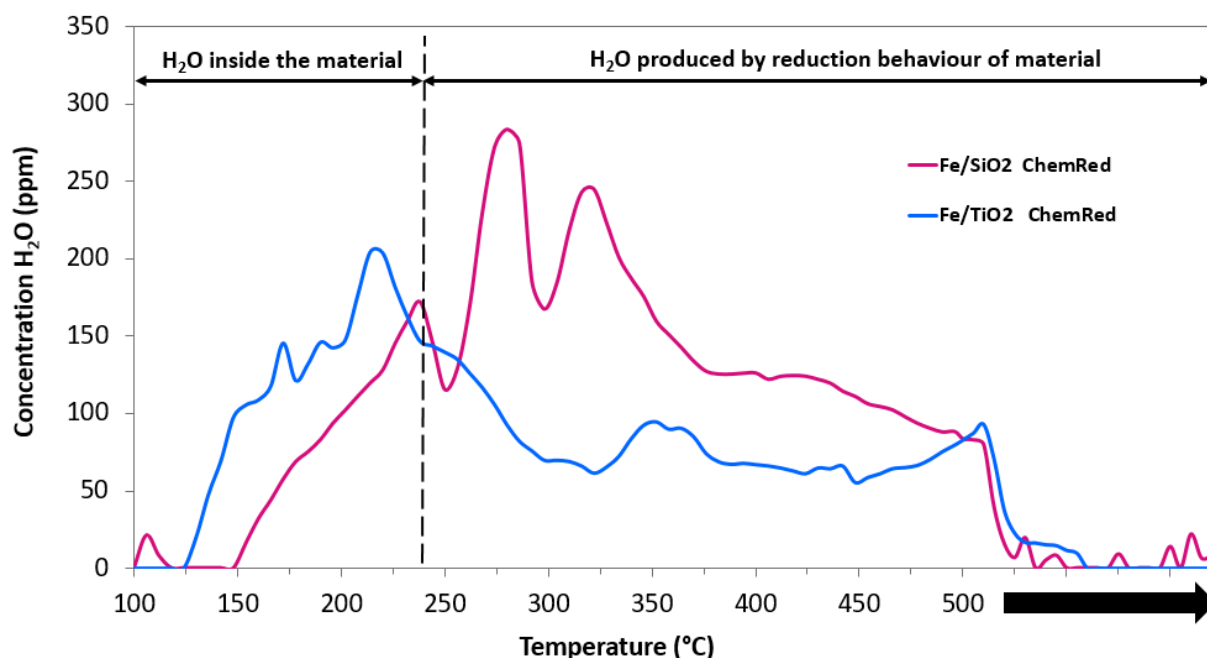

Figure 4.2. TPR at 500 °C of Fe(II)/TiO₂ and Fe/SiO₂ samples

Next, reduction behaviours up to 400 °C of both TiO$_2$ supported monometallic Zn and Fe and bimetallic Fe-Zn 1:5 catalysts and reduction behaviour up to 500°C of TiO$_2$ supported bimetallic Fe-Zn 1:1 are plotted in *(Figure 4.3)*. Zn/TiO$_2$ sample only shows limited H$_2$O formation above 250°C whereas Fe-Zn 1:1/TiO$_2$ presents high amounts of water under heating up to 500 °C, exceeding the expected water production corresponding to full reduction of iron oxide *(Table 4.5)*. This is probably related to the reduction and then evaporation of zinc at such high temperature as revealed by XRF analyses and noticed by the observation of a metallic deposit at the outlet of the reactor. When the reduction temperature is limited at 400°C, the water production is lower but still a little larger than the expected

one *(Table 4.5)* which might indicate a limited reduction of zinc oxide in addition to the one of iron oxide.
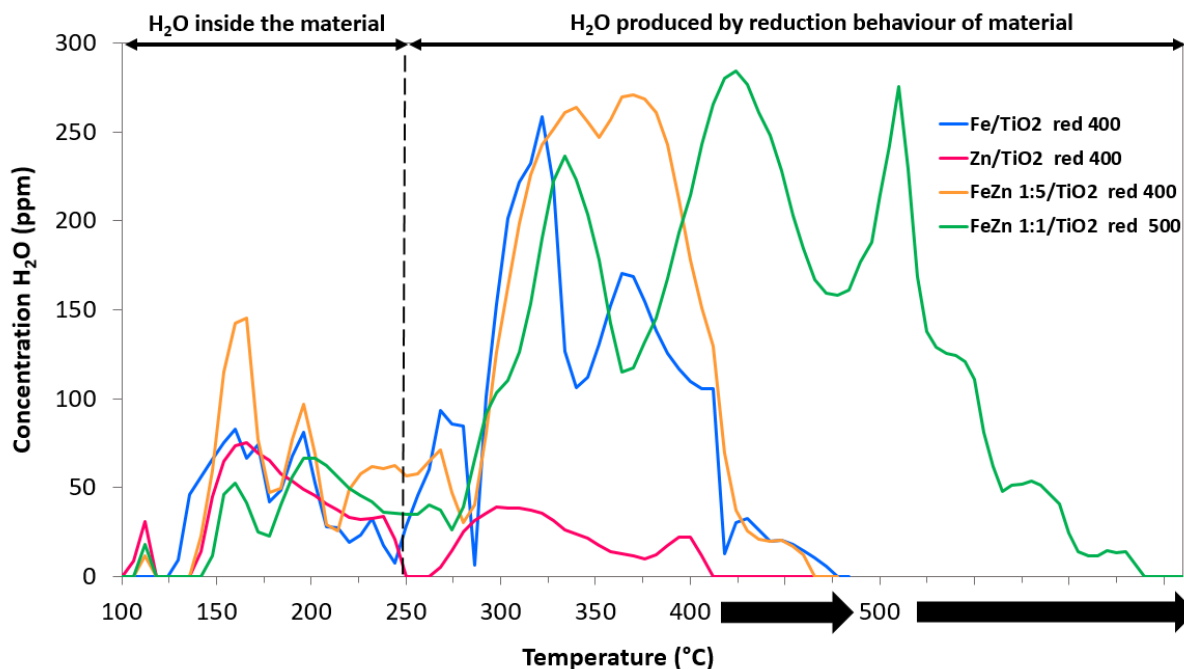

Figure 4.3. TPR at 400 °C of Fe(II)/TiO$_2$, Zn/TiO$_2$ and FeZn 1:5/TiO$_2$ and TPR at 500 °C of FeZn 1:5/TiO$_2$ samples synthesised by DPu

4.1.3.   X-Ray Diffraction (XRD)

Phase identification of as-prepared and activated samples is described in this section.

○ *Fe/TiO$_2$ sample by Deposition-precipitation with urea*

In Fe/TiO$_2$ material prepared by DPu, the majority of the peaks detected by XRD *(Figure 4.4)*. correspond to the TiO$_2$ support phases, anatase and rutile, whose most intense peaks are found in 2θ positions at 25°, 47.5°, 54°, 55° and 63° in the case of anatase and at 26.5°, 36°, 41° and 56.5° for rutile phase. Calcination treatment has no significant effect on the structure of the iron-based catalyst. On the other hand, metallic iron has been the only iron phase visible at 44.8° by XRD in the reduced sample at 400 °C.

The crystallite size of this metallic iron was estimated by the Scherrer's equation obtaining a value around 25 nm.
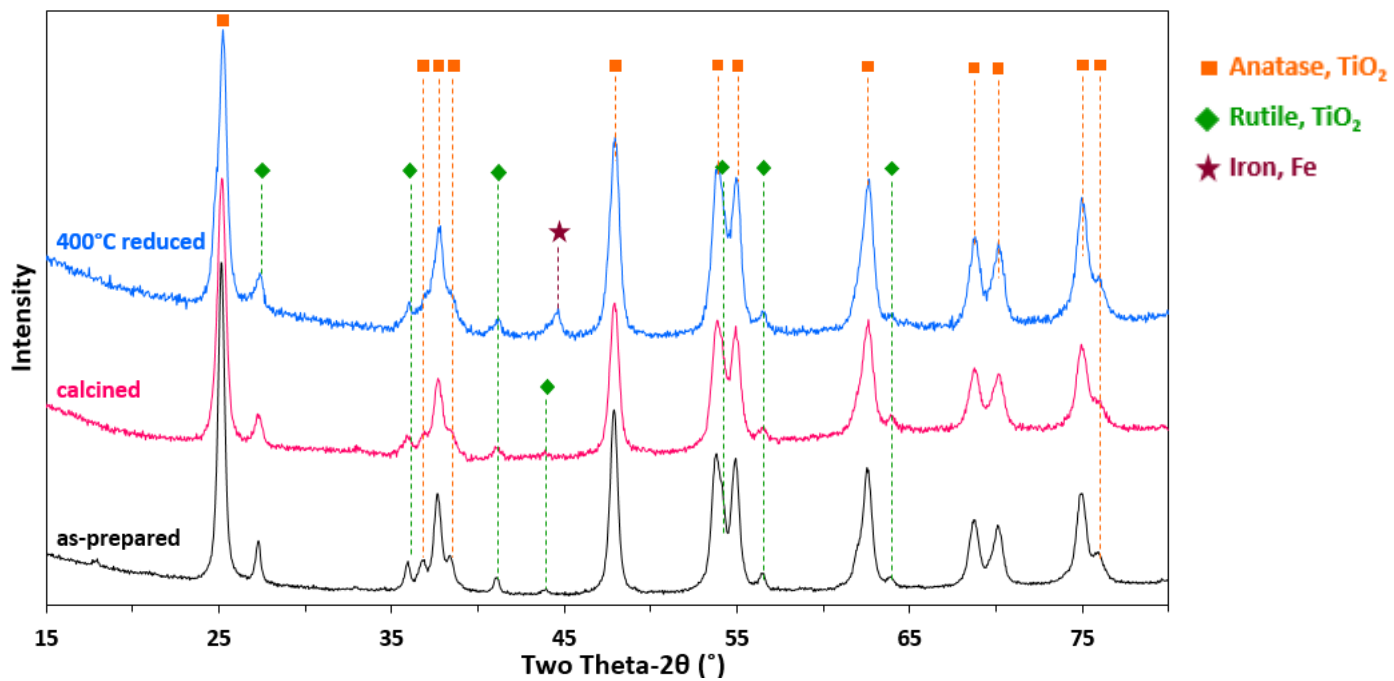
Figure 4.4. XRD patterns of as-prepared (black), calcined (pink) and reduced at 400 °C (blue) Fe(II)/TiO$_2$ samples synthesised by DPu

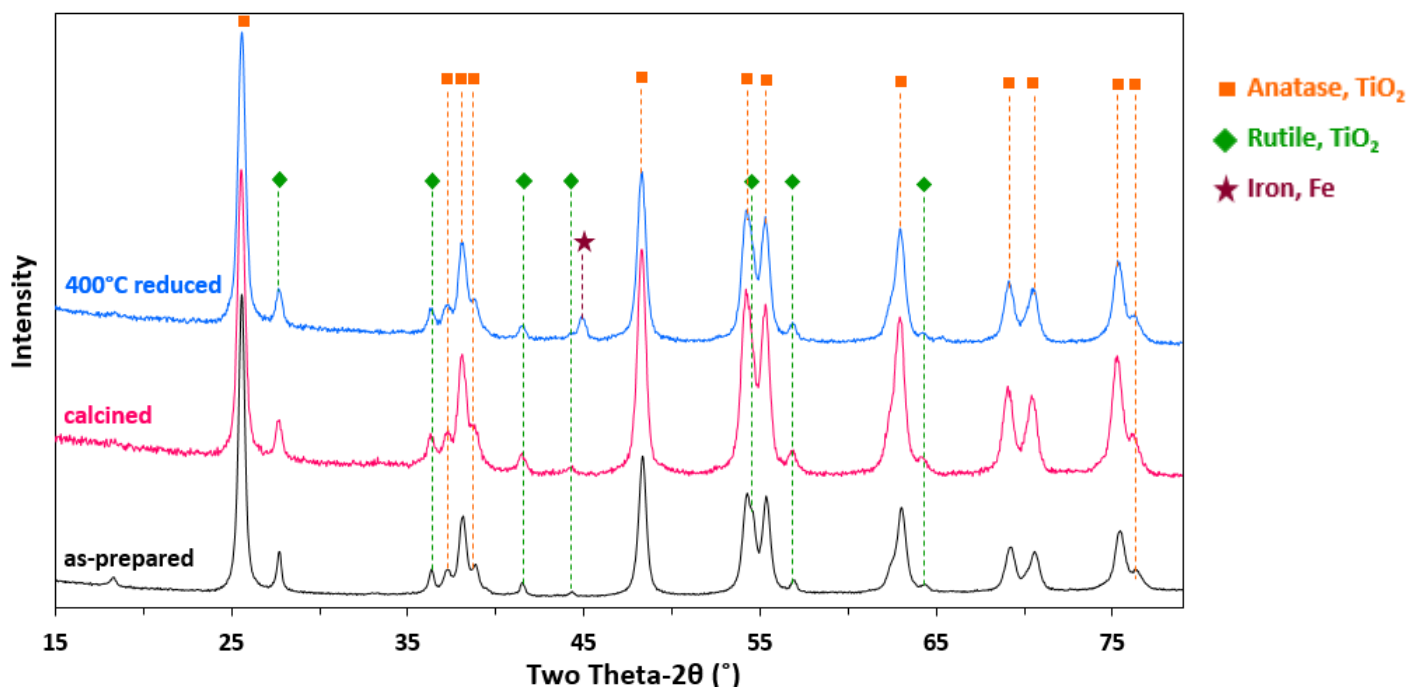   o   **Fe-Zn 1:1/TiO$_2$ sample by Deposition-precipitation with urea**

There are no relevant changes in the structure of the sample after comparing the graph to that of monometallic Fe/TiO₂ catalyst. Only metallic iron has been detected at 44.8° with smaller crystallite size, 28 nm. No zinc oxide phase could be observed which might be due to high dispersion and/or too small crystallite size *(Figure 4.5)*.

○ ***Fe-Zn 1:5/TiO₂ sample by Deposition-precipitation with urea***
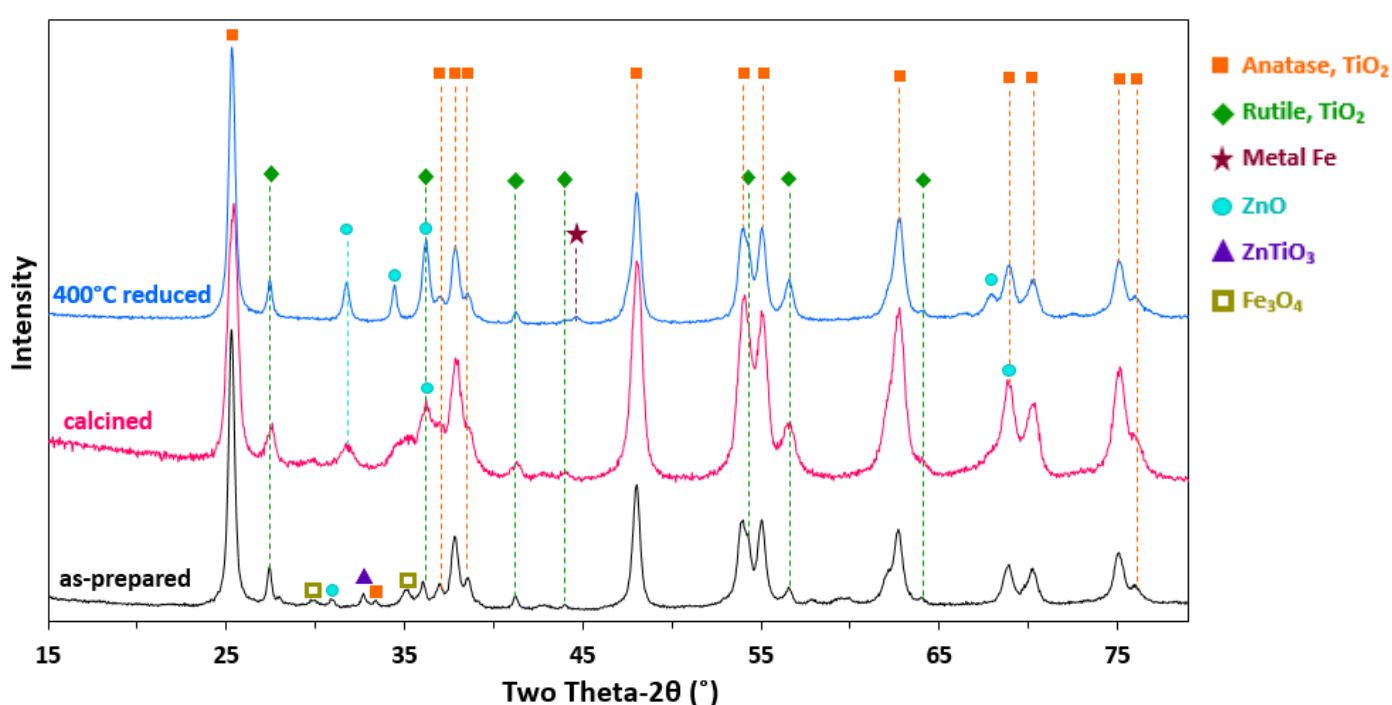

Figure 4.6. XRD patterns of as-prepared (black), calcined (pink) and reduced at 400 °C (blue) Fe(II)Zn 1:5/TiO₂ samples synthesised by DPu

The TiO₂ supported Fe-Zn 1:5 catalyst prepared by DPu exhibits a larger variety of compounds *(Figure 4.6)* though some of them could not be identified because of overlapped peaks or weak intensity. It is underlining the presence of zinc oxide (ZnO), especially after reduction treatment at 400°C. In addition, traces of iron oxide are detected in the as-prepared sample referring to the two very weak peaks at ≈30°and ≈35° and there is also probably a species of zinc titanium oxide. After reduction at 400°C, the metallic iron peak identified at 44.8° is weak with a crystallite size estimated around 31 nm.

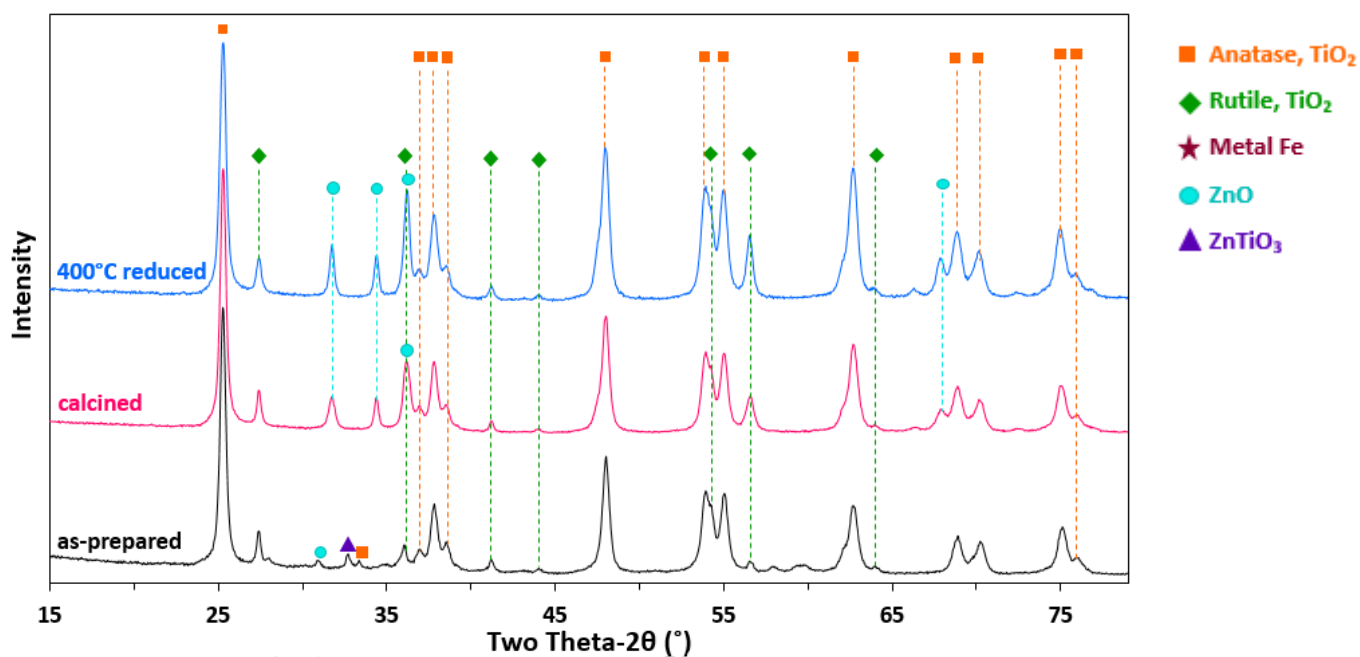o **_Zn/TiO₂ sample by Deposition-precipitation with urea_**

Figure 4.7. XRD patterns of as-prepared (black), calcined (pink) and reduced at 400 °C (blue) Zn(12wt%)/TiO₂ samples synthesised by DPu

The monometallic Zn(12wt%)/TiO₂ catalyst shows approximately the same compounds as the bimetallic FeZn1:5/TiO₂ apart from the absence of iron oxide and metallic iron *(Figure 4.7)*. The elevated amount of Zn leads again to the detection of zinc oxide peaks.
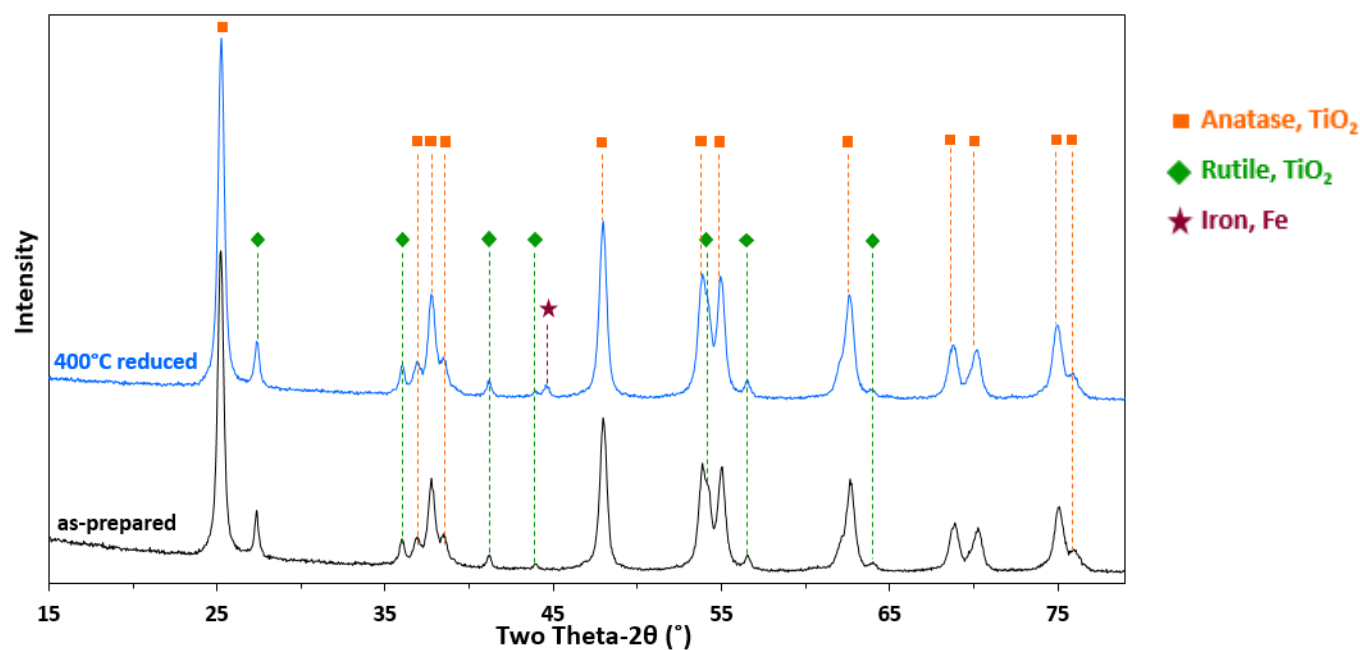
o **_Fe/TiO₂ sample by Chemical Reduction_**

Figure 4.8. XRD patterns of as-prepared (black) and reduced at 400 °C (blue) Fe(II)/TiO₂ samples synthesised by Chemical Reduction

The pattern of Fe/TiO$_2$ sample synthesised by Chemical Reduction *(Figure 4.8)*. is quite similar to the one obtained by DPu apart from the lower intensity of metallic iron peak at approximately 45°. Crystallite size calculated by Scherrer's equation is 49 nm.

- ○ *Fe/SiO$_2$ sample by Chemical Reduction*

As SiO$_2$ is an amorphous material, no diffraction peak from the support is observed except the broad peak at 22°. As XRF demonstrated, there should be iron species in the as-prepared sample but because of its small size or due to being amorphous, nothing has been identified. Nonetheless, after the reduction treatment, metallic iron is perfectly distinguished at 44.6° *(Figure 4.9)*. with a crystallite size of 26 nm obtained by Scherrer's equation.
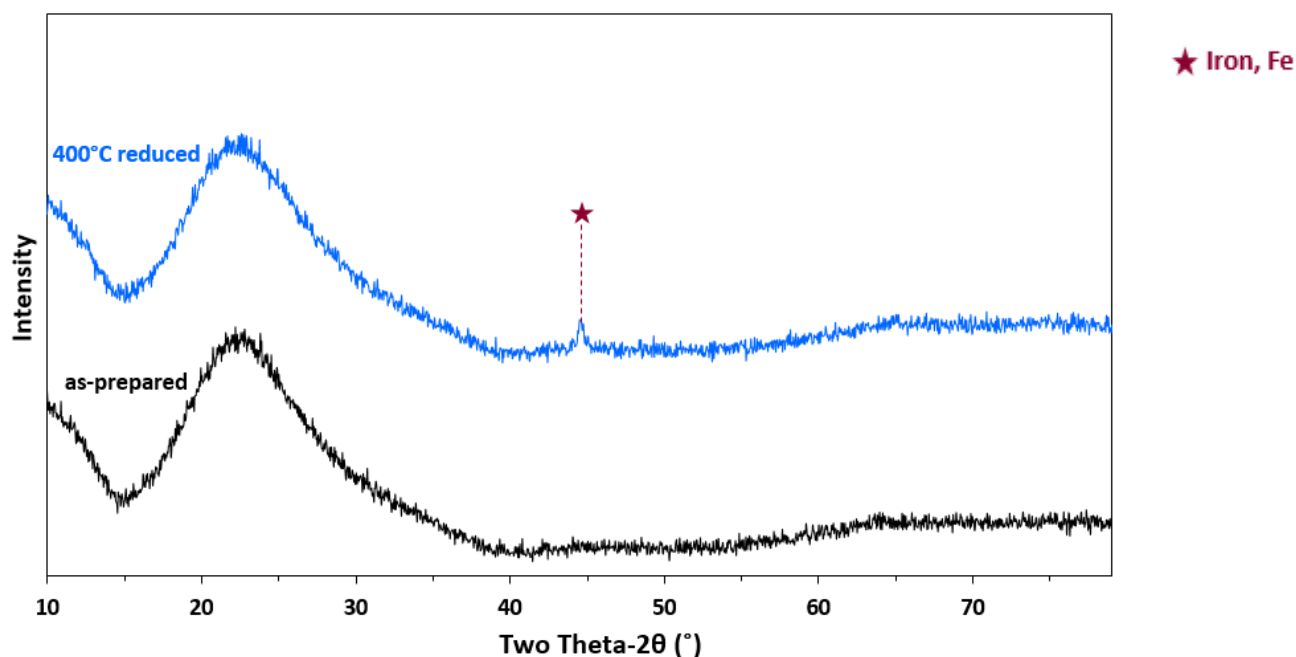

Figure 4.9. XRD of as-prepared (black) and reduced at 400 °C (blue) Fe(II)/SiO$_2$ samples synthesised by Chemical Reduction

- ○ *Fe-Zn 1:5/TiO$_2$ sample by Chemical Reduction*

In spite of the fact that bimetallic FeZn 1:5/TiO$_2$ catalyst synthesised by Chemical reduction was not subjected to a calcination before reduction at 400 °C, characteristic peaks of zinc oxide are visible after reduction *(Figure 4.10)*. In addition, the intensity of the metal iron peak is higher than for the sample prepared by DPu and presents smaller crystallite size, around 27 nm.
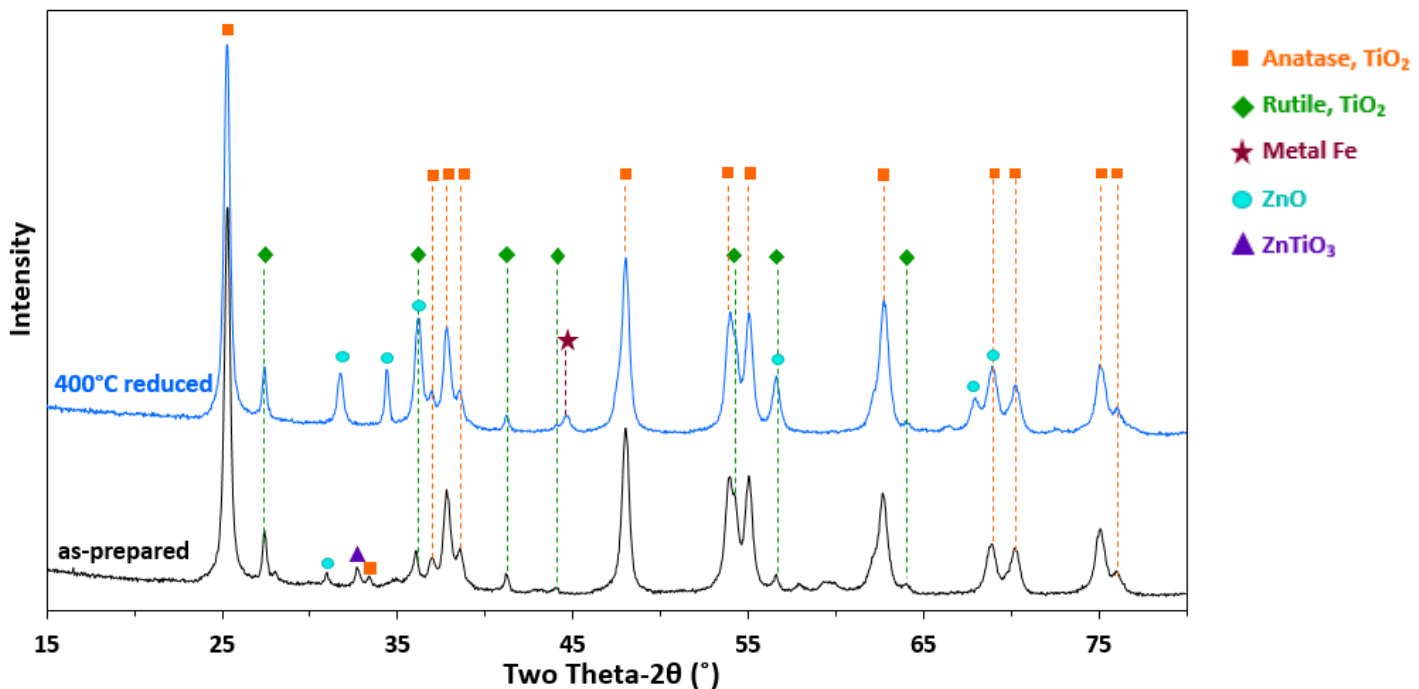
Figure 4.10. XRD of as-prepared (black) and reduced at 400 °C (blue) Fe-Zn 1:5/TiO$_2$ samples synthesised by Chemical Reduction

4.1.4. Transmission Electron Microscopy (TEM)

In order to complement the information deduced by the other techniques, morphological and structural analyses were performed using TEM on three of the synthesised samples. Before microscopy analysis, a calcination treatment at 400 °C for 2h (heating rate: 5°C/min) followed by a reduction treatment under H$_2$ at 400 °C for 2h (heating rate: 3°C/min) were performed for Fe/TiO$_2$ and Fe-Zn 1:5/TiO$_2$ samples prepared by DPu. On the other hand, the Fe/TiO$_2$ sample synthesised by Chemical reduction was only subjected to the reduction treatment under the same conditions. This pre-treatment was undertaken so as to test the materials after the same activation procedure as for the catalytic tests.

o **Fe/TiO$_2$ sample by Chemical Reduction**

Several areas were analysed by TEM along with dark field imaging (HAADF) and Elemental mapping to deepen the analysis. Presence of iron after reduction was observed by XRD so it was supposed that Fe crystallites were large enough to be detected by TEM. Unfortunately, it is not possible to gain so much information from bright and dark field TEM images since the majority of particles look very similar as

the molecular weights of Ti and Fe are rather close so the main principle of Z-contrast technique based on the statement of the higher the atomic number the brighter image is hardly useful. However, as far as it is appreciated in the elemental mapping of Fe *(Figure 4.11)*, the iron species appear well dispersed on the support throughout the sample without any clear presence of cluster or agglomeration.
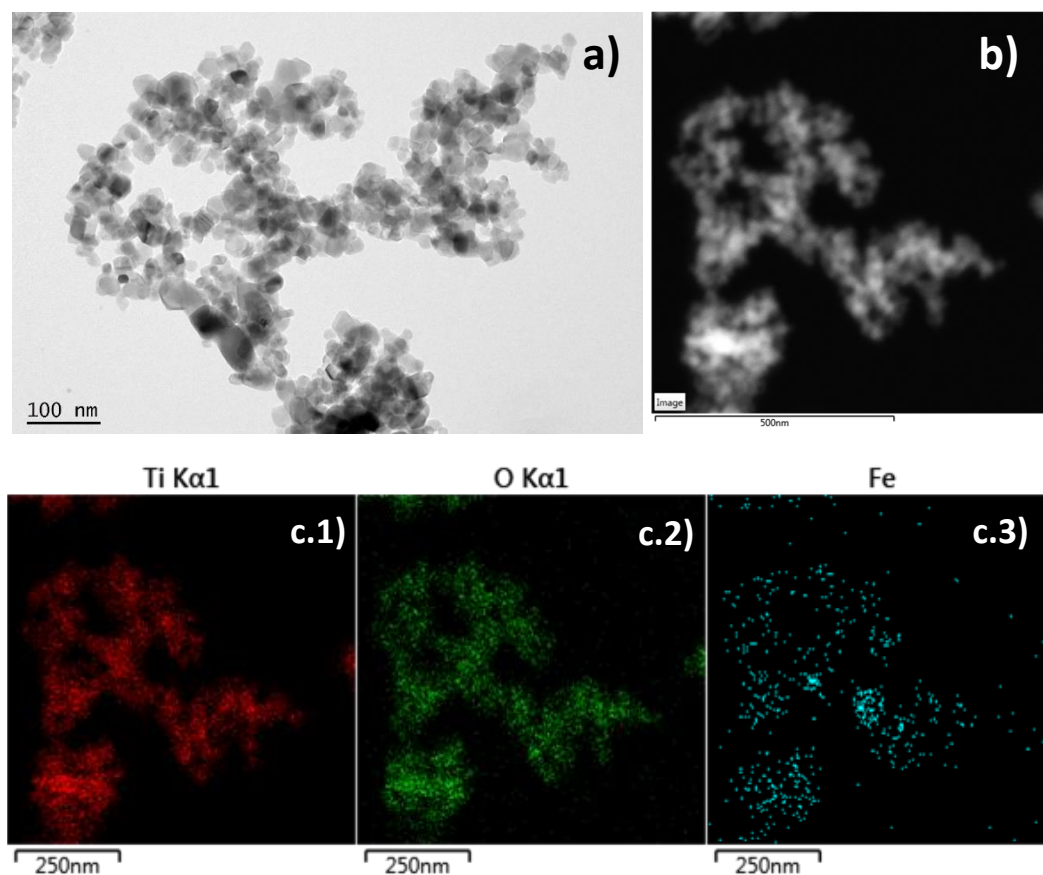

Figure 4.11. Spectre 1 of Fe/TiO$_2$ sample (Chemical Reduction): a) TEM bright field graph b) STEM-HAADF and c) Elemental mapping of c.1) Ti, c.2) O, c.3) Fe

Nonetheless, in the case of other images corresponding to another area of the sample, the elemental mapping results are consistent with the XRD results obtained. Both show that the sample also contain large particles of iron as it can be observed in *(Figure 4.12)*.
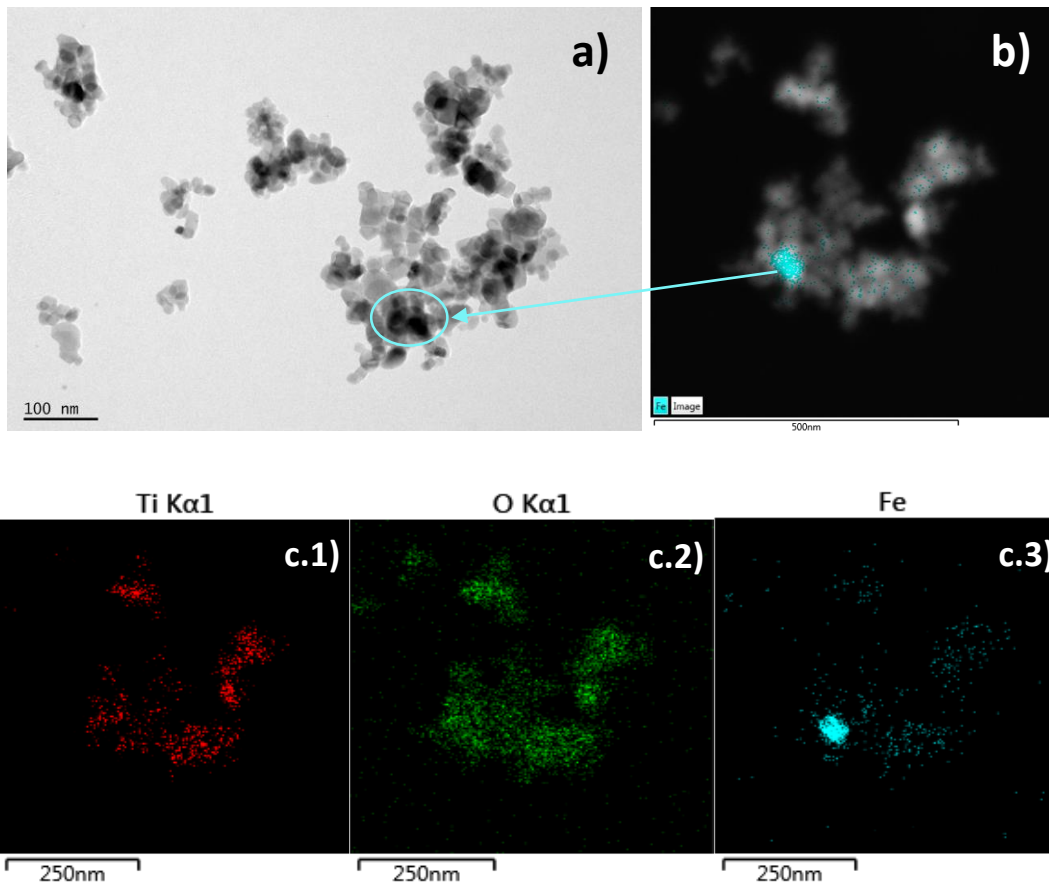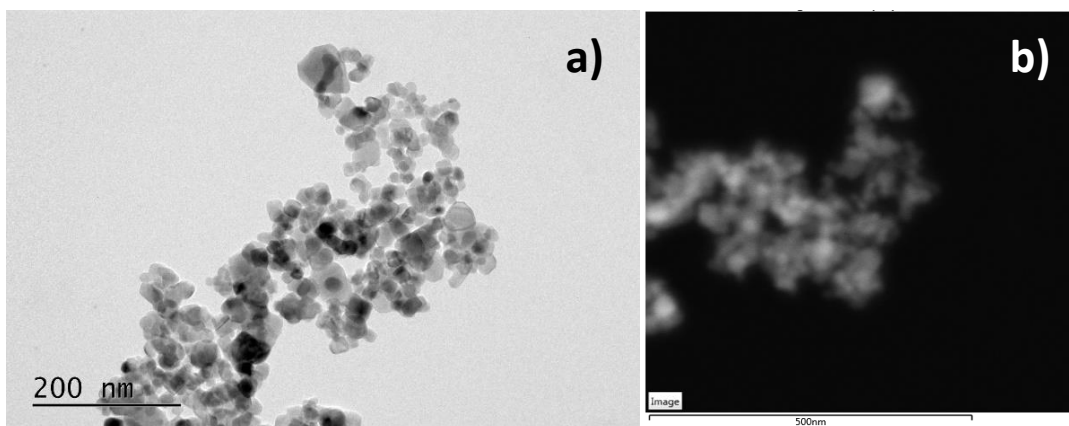
Figure 4.12. Spectre 2 of Fe/TiO$_2$ sample (Chemical Reduction): a) TEM bright field graph b) STEM-HAADF and c) Elemental mapping of c.1) Ti, c.2) O, c.3) Fe

    o   ***Fe/TiO$_2$ sample by Deposition-precipitation with urea***

TEM and HAADF images of the Fe/TiO$_2$ sample prepared by DPu also display particles of similar size and aspects throughout all the sample. By means of elemental mapping, it is possible to identify iron species very well dispersed on the surface of the support. The presence of Fe clusters has not been found in this case since all the elements seem uniformly distributed throughout the material.
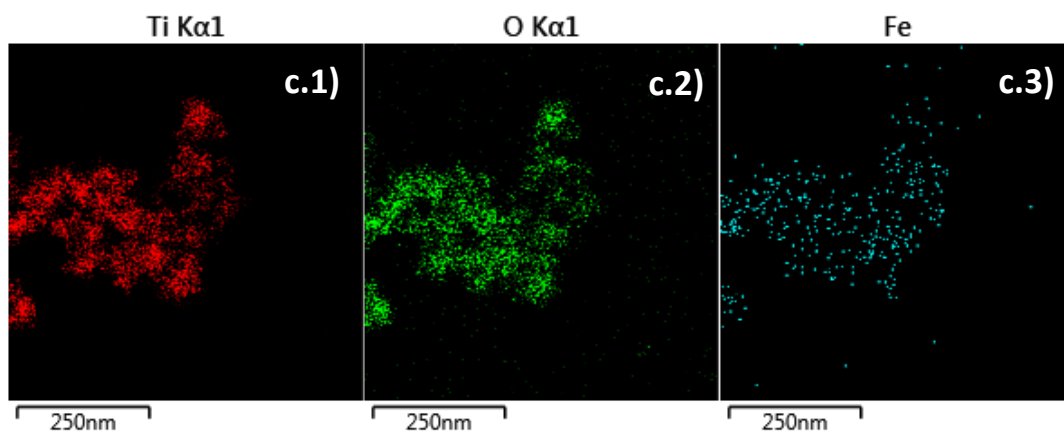
Figure 4.13. Spectre 1 of Fe/TiO$_2$ sample (DPu): a) TEM bright field graph b) STEM-HAADF and c) Elemental mapping of c.1) Ti, c.2) O, c.3) Fe

- **Fe-Zn 1:5/TiO2 sample by Deposition-precipitation with urea**

The bimetallic catalyst shows a more complicated structure and, for that reason, an EDX analysis has been coupled with TEM imaging. As it can be observed in *Tables b) and c)* attached in *(Figure 4.14)*, different regions of the sample do not have the same composition. For instance, referring to atomic percent calculated by EDX, *region 1* is mainly formed by TiO$_2$ support whereas *region 2* mostly contains zinc oxide corroborating XRD results.

b)

Element	% atomic
O	77.86
Si	0.16
Ca	0.18
Ti	21.23
Fe	0.23
Zn	0.33

c)

Element	% atomic
O	63.47
Si	0.15
Ti	1.47
Cr	0.07
Fe	1.66
Zn	33.18

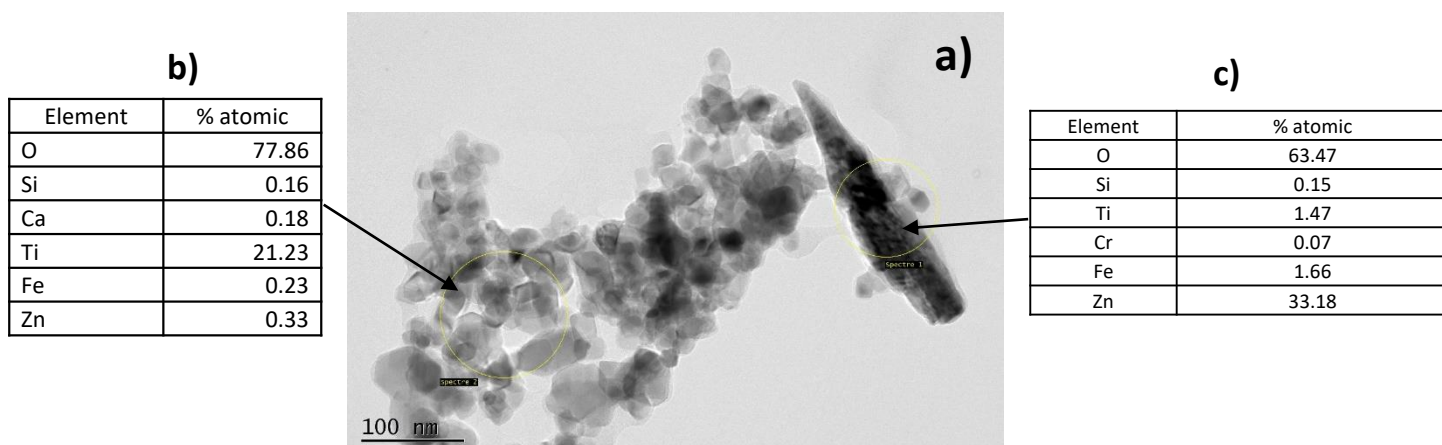**Figure 4.14.** Spectre 1 of Fe-Zn 1:5/TiO$_2$ sample (DPu): a) TEM bright field graph, b) EDS of region 1 and c) EDS of region 2

Moreover, by means of elemental mapping, different compositions of various areas can be also demonstrated. *Figure 4.15. c.3)* shows a zone with a high concentration of well dispersed Zn which probably corresponds to a zinc oxide region. On the other hand, iron appears globally well dispersed

throughout the material as well as the presence of some Fe agglomerations is also detected *Figure 4.15. c.4)*.

Figure 4.15. Spectre 2 of Fe-Zn 1:5/TiO$_2$ sample (DPu): a) TEM bright field graph b) STEM-HAADF and c) Elemental mapping of c.1) Ti, c.2) O, c.3) Zn, c.4) Fe

On the other hand, in *Figure 4.16*, zinc seems to be well dispersed on the surface of the TiO$_2$, support *(Figure 4.16. c.3))* and Fe presents a good dispersion but some clusters of iron can be also detected *(Figure 4.16. c.4))*.
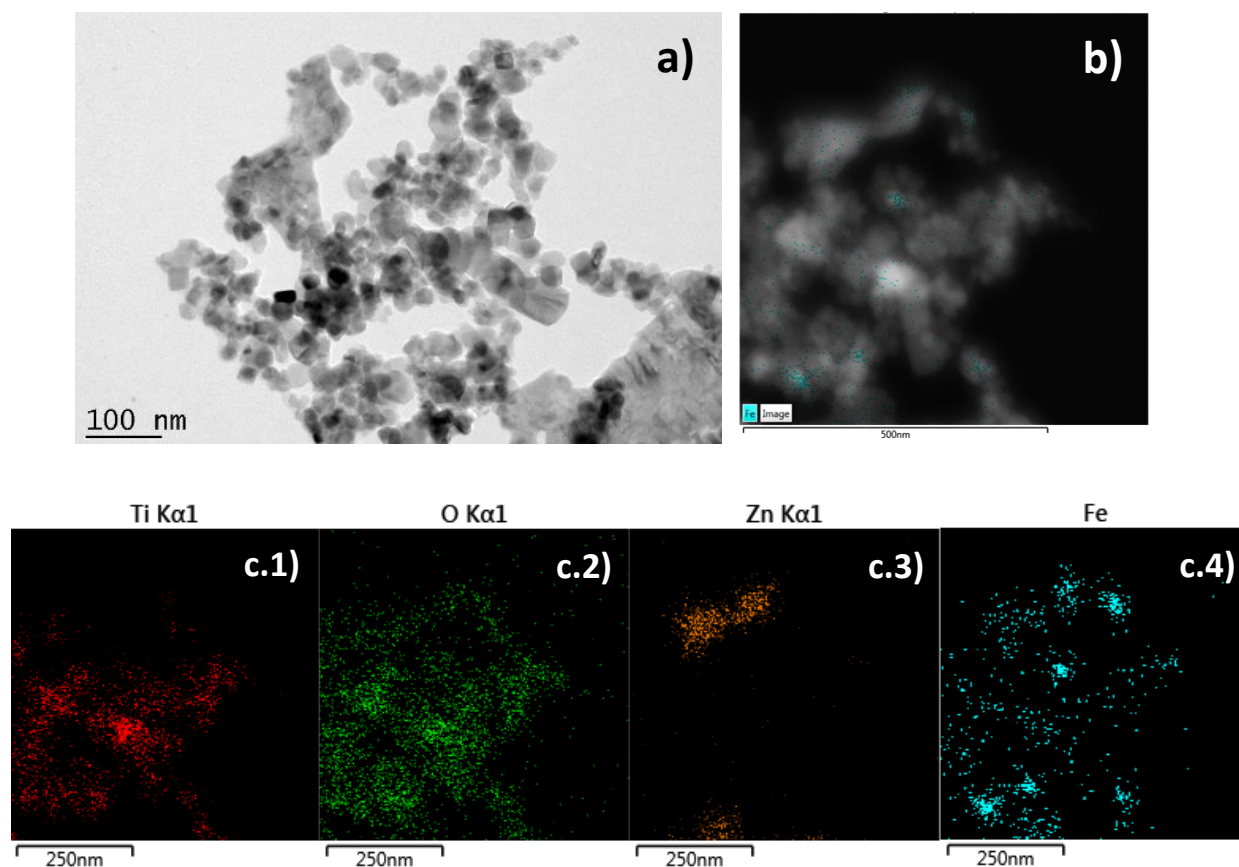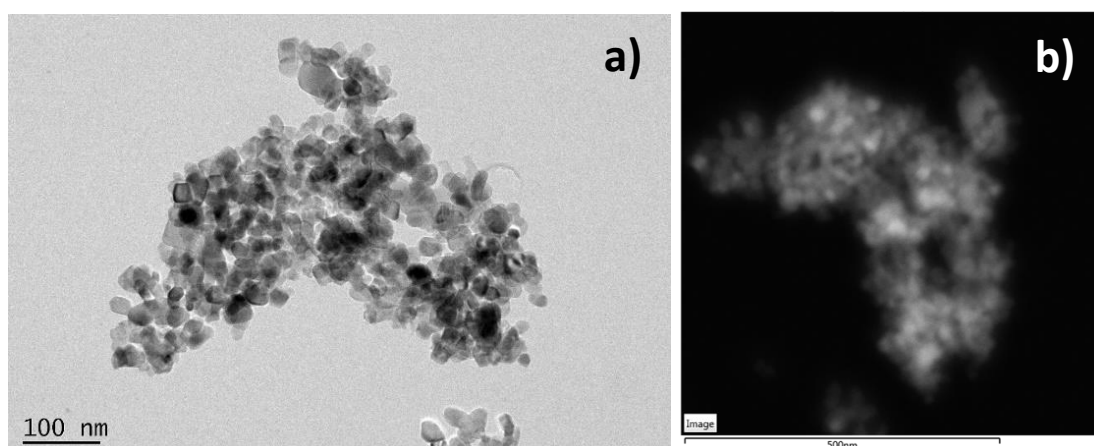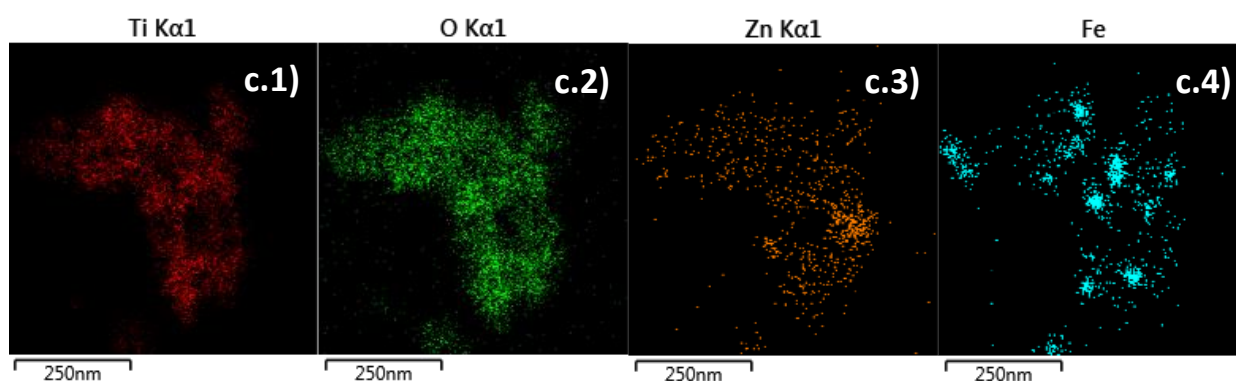
Figure 4.16. Spectre 3 of Fe-Zn 1:5/TiO$_2$ sample (DPu): a) TEM bright field graph b) STEM-HAADF and c) Elemental mapping of c.1) Ti, c.2) O, c.3) Zn, c.4) Fe

➢ *__Characterization conclusions__*

First of all, XRF results confirmed that the amounts of Fe and Zn obtained experimentally mostly agreed with the expected loadings, with the exception of samples containing Zn which showed an important loss of Zn after reduction at 500 °C. This fact was also evinced by TPR results of Fe-Zn 1:1/TiO$_2$ depicted in *Figure 4.3* with an extra amount of water produced when reduction takes place up to 500 °C. Despite the fact that TPR results indicate that reduction up to 400 °C results in an incomplete reduction for Fe/TiO$_2$ by comparison with reduction at 500 °C, reduction at the lowest of the two temperatures will be privileged for activation before catalytic reaction in order to limit the loss of Zn during the thermal treatment.

On the other hand, by XRD analyses, metallic iron is identified after reduction at 400°C in all the tested samples which should mean the presence of large particles in the material. This could be demonstrated in some samples by means of TEM imaging which showed the presence of Fe agglomerations as well as the one of dispersed iron throughout the sample. In addition, for the highly Zn loaded Fe-Zn 1:5 sample, elemental mapping of the material evinced the presence of zinc oxide, also detected by XRD, as well as some regions where Zn is as well dispersed as Fe. Thus, it can be deduced by TEM images that Zn and Fe are in proximity of each other although the existence of any mixed phase could not be evidenced.

4.2. CATALYTIC PERFORMANCE

The samples were tested in the reaction of selective hydrogenation of 1,3-butadiene in an excess of propene (propene/butadiene ratio=100) after activation under H_2 at 400°C. The evolution of the concentration of butadiene, i.e., butadiene conversion, and of the alkanes formation to estimate the selectivity will be reported as a function of the reaction time.

4.2.1. Monometallic Fe/TiO₂ comparison

First of all, the catalytic performance of 50 mg of monometallic Fe/TiO_2 prepared by DPu after calcination and reduction at both 400°C and 500°C for 2 h was evaluated and gathered in *Figure 4.17*. Initially, three analyses were carried out at room temperature. Then, the reactor was heated from 30°C to 200°C (heating rate: 2°C/min). These experiments are displayed in a zoom in *Figure 4.18* where it is observed that the butadiene conversion profile is very similar for both cases with a rather rapid deactivation during reaction at room temperature. However, over approximately 20 hours at 200 °C, the two samples behaviours in terms of butadiene concentration are different. After reaching a maximum butadiene conversion at 200°C, a progressive deactivation is observed for both samples but the Fe/TiO_2 catalyst with a pre-treatment at 400 °C presents higher butadiene conversion although the iron reduction is supposed incomplete making reference to TPR results.
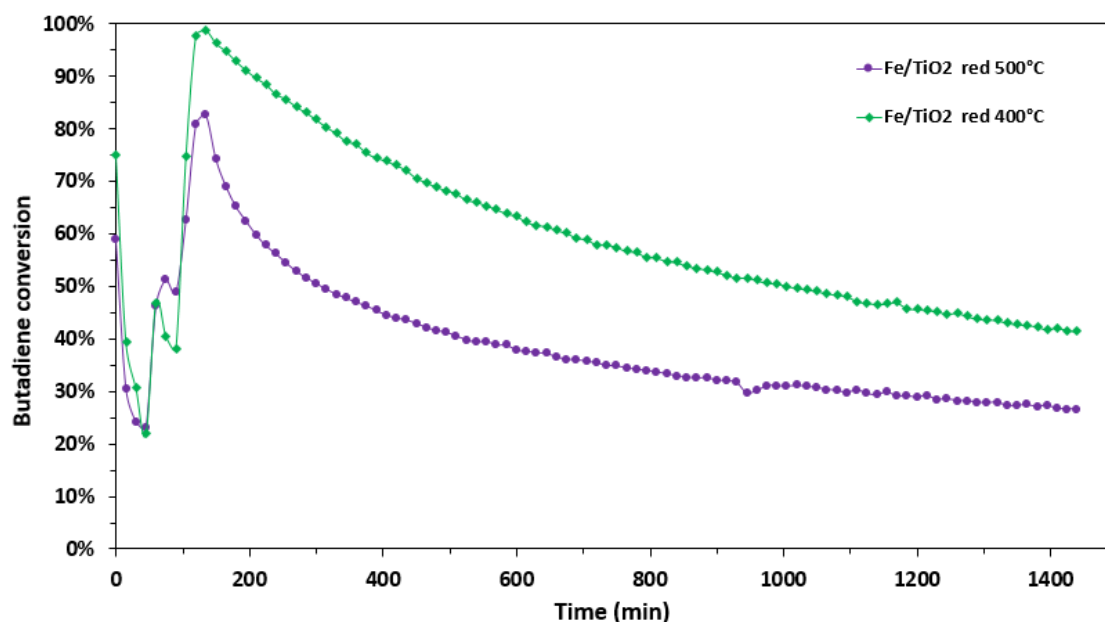
Figure 4.17. Butadiene conversion as a function of the time over Fe/TiO_2 activated at 500°C (on purple) and Fe/TiO_2 activated at 400°C (green) (DPu)

Figure 4.18. Zoom in Figure 4.17 between 0-140 minutes. Representation of butadiene conversion over reaction temperature

On the other hand, the selectivity can be analysed by checking the alkanes (butane and propane) formation. Both cases are alike but, at the beginning, higher selectivity is observed for sample activated at 400 °C though a slight change happens when both remain at 200 °C with the sample activated at 500°C being the most selective. However, it is worth to note that the alkanes production is very low (below 3000 ppm at maximum) whatever the reduction temperature, underlining the fact that iron is very selective to alkenes in this reaction.
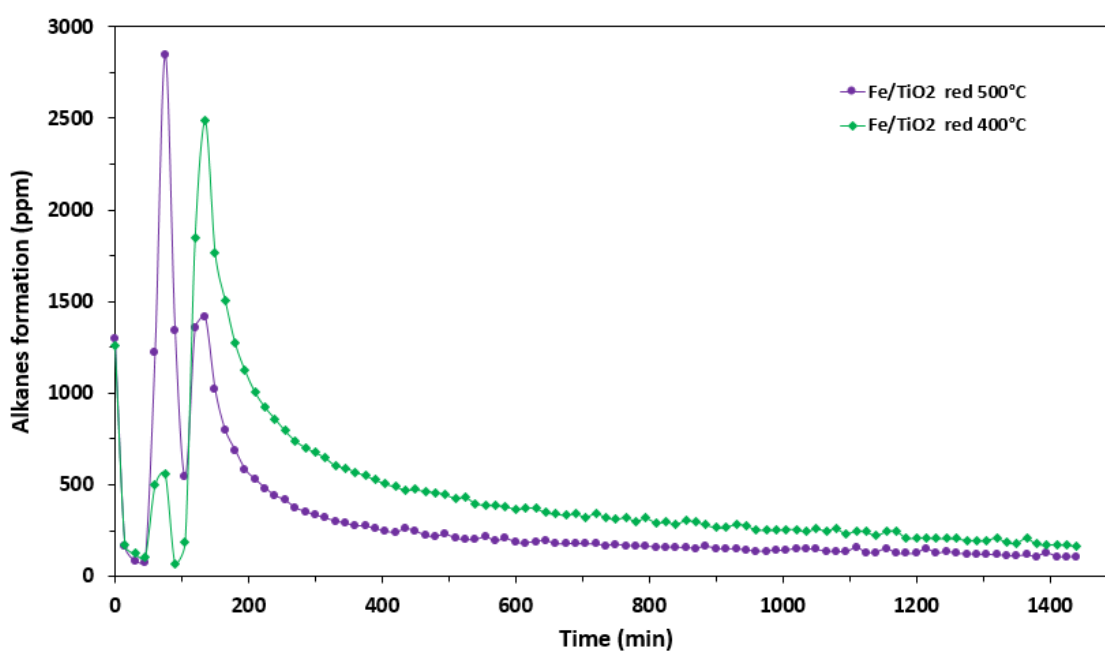
Figure 4.19. Alkanes formation as a function of the time over Fe/TiO$_2$ activated at 500°C (on purple) and Fe/TiO$_2$ activated at 400°C (green) (DPu)

4.2.2. Comparison between samples prepared by Deposition-precipitation with urea

Secondly, all catalytic results of samples synthesised by Deposition-precipitation with urea and calcined then reduced at 400°C are depicted together in *Figure 4.20* and *Figure 4.22*. As in the previous case, the temperature programmed reaction was carried on the reduced 50 mg of catalysts after three analyses at room temperature and, then, the temperature for the catalytic reaction was kept as a constant for 20 h when 200 °C was reached.

Undoubtedly, bimetallic Fe-Zn 1:5/TiO$_2$ is more active and stable at 200°C than the other catalysts. Even the sample with a Fe-Zn molar ratio of 1:1 presents a higher activity than monometallic Fe/TiO$_2$ and Zn(12wt%)/TiO$_2$ which gives rise to the conclusion that Zn addition increases the catalytic activity and stability of iron catalysts in selective hydrogenation. It should also be pointed out that the monometallic Zn/TiO$_2$ turned out to be quite active especially when the final temperature was reached.
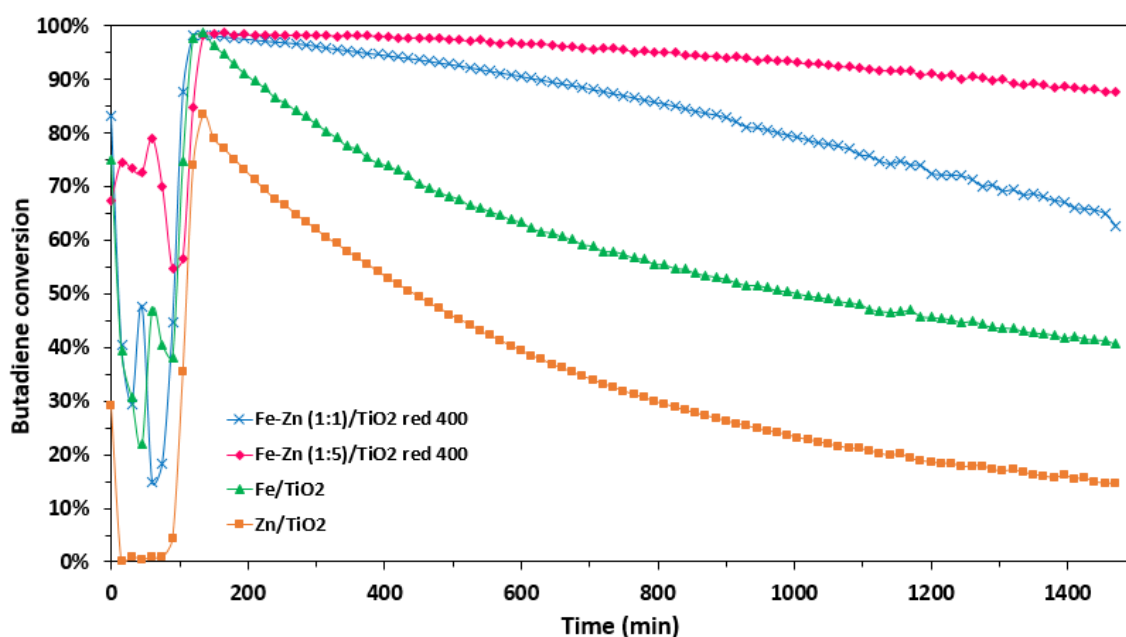
Figure 4.20. Butadiene conversion as a function of the time over Fe/TiO$_2$ (green), Zn/TiO2 (orange), Fe-Zn 1:1/TiO$_2$ (blue) and Fe-Zn 1:5/TiO$_2$ (pink). All samples synthesised by DPu and previously calcined and reduced at 400 °C

Focusing on the first experiments undertaken at room temperature and during the increase in temperature *(Figure 4.21)*, it is remarkable that the bimetallic Fe-Zn 1:5/TiO$_2$ was the most active and also stable from the starting point.
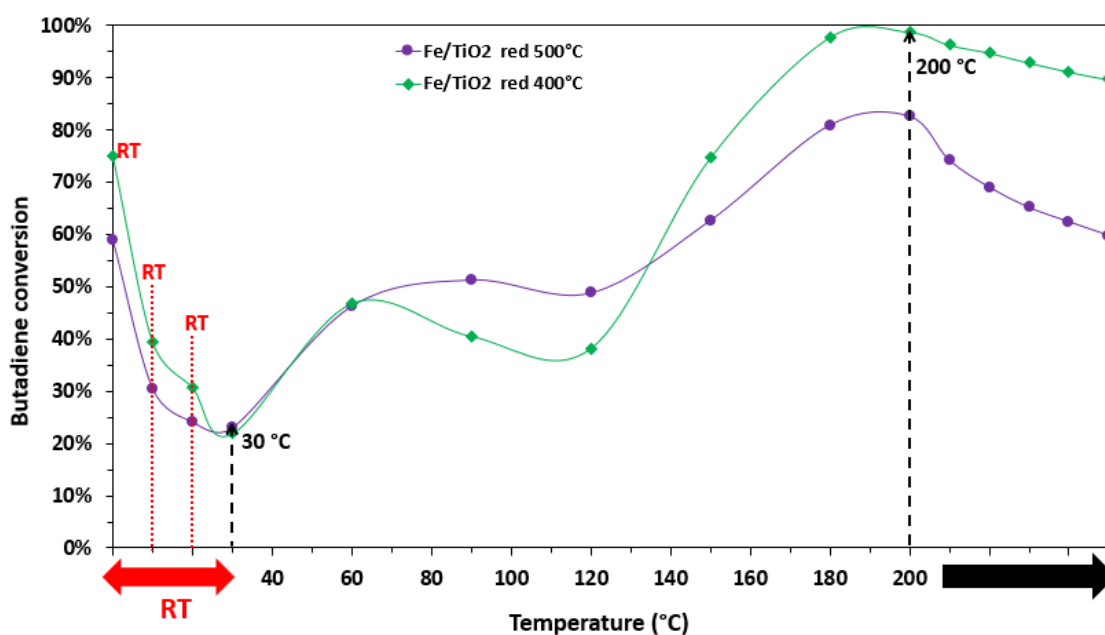
Figure 4.21. Zoom in Figure 4.20 between 0-140 minutes. Representation of butadiene conversion over reaction temperature

However, regarding the formation of alkanes, the bimetallic Fe-Zn 1:5/TiO$_2$ presents the highest alkanes production, thus the lowest selectivity to alkenes, but it can still be considered as highly selective as the alkanes concentration at the outlet is very low, especially when the reaction temperature is stabilized at 200 °C (less than 2000 ppm). From a general point of view, the four samples prepared by DPu show similar behaviours with regard to alkenes selectivity reaching more than 99%.
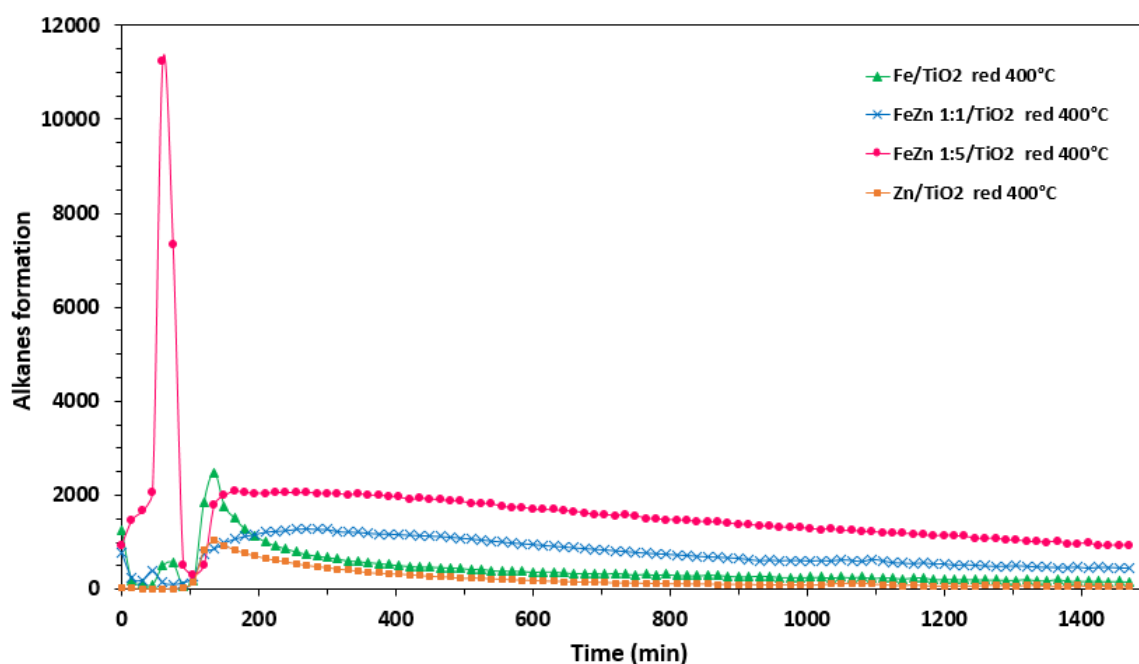
Figure 4.22. Alkanes formation as a function of the time over Fe/TiO$_2$ (green), Zn/TiO$_2$ (orange), Fe-Zn 1:1/TiO$_2$ (blue) and Fe-Zn 1:5/TiO$_2$ (pink). All samples synthesised by DPu and previously calcined and reduced at 400 °C.

4.2.3. Comparison between samples prepared by Chemical Reduction

In addition, the catalytic performances of TiO_2 supported monometallic Fe(II) and bimetallic Fe-Zn 1:5 and SiO_2 supported monometallic Fe(II) prepared by chemical reduction, after reduction at 400°C for 2 h, are depicted in *Figure 4.23*. Despite the fact that Fe/SiO_2 showed a higher Fe content than Fe/TiO_2, it presents the lower catalytic activity in selective hydrogenation of 1,3-butadiene. On the other side, the monometallic Fe/TiO_2 exhibited a slightly lower activity than the equivalent samples synthesised by DPu but presents an increase in stability with time. The most active and stable material is again the bimetallic Fe-Zn 1:5/TiO_2 since complete butadiene conversion is reached at 200 °C and remained for 2 h underlining an improved stability.
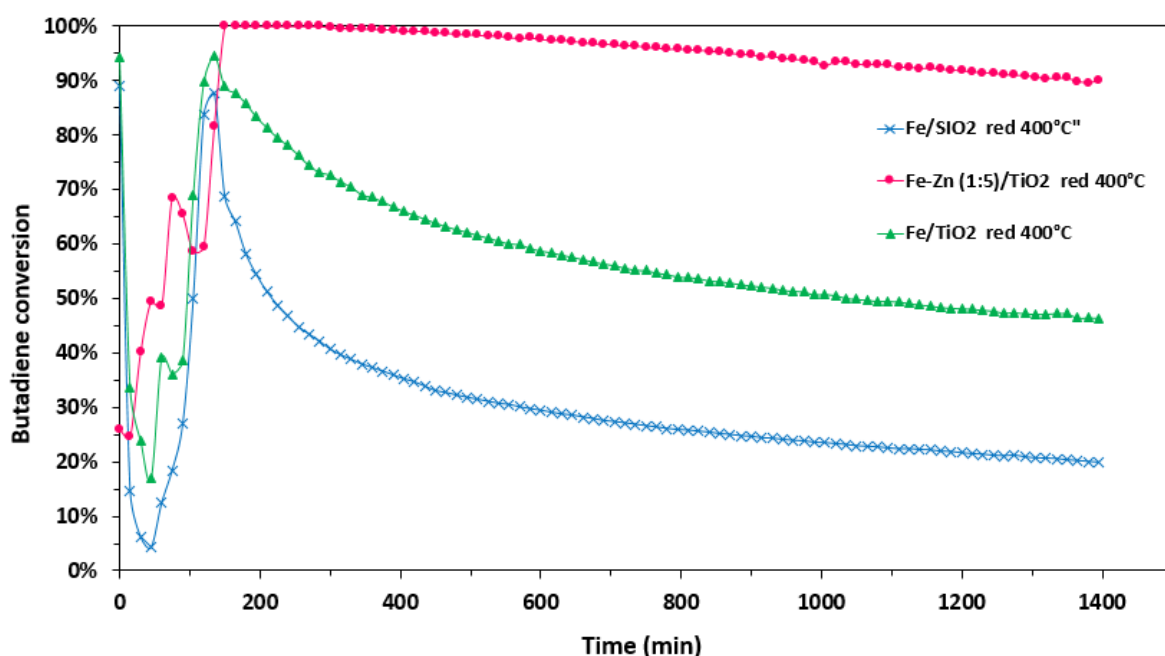
Figure 4.23. Butadiene conversion as a function of the time over Fe/TiO_2 (green), Fe/SiO_2 (blue) and Fe-Zn 1:5/TiO_2 (pink). All samples synthesised by Chemical Reduction and previously reduced at 400 °C

Referring to the initial analyses, the butadiene conversion over bimetallic Fe-Zn 1:5/TiO_2 presents a peculiar behaviour as it was first rather low (25%) but was increasing with time at RT while the monometallic catalysts have high initial conversion, then deactivated rapidly *(Figure 4.24)*.
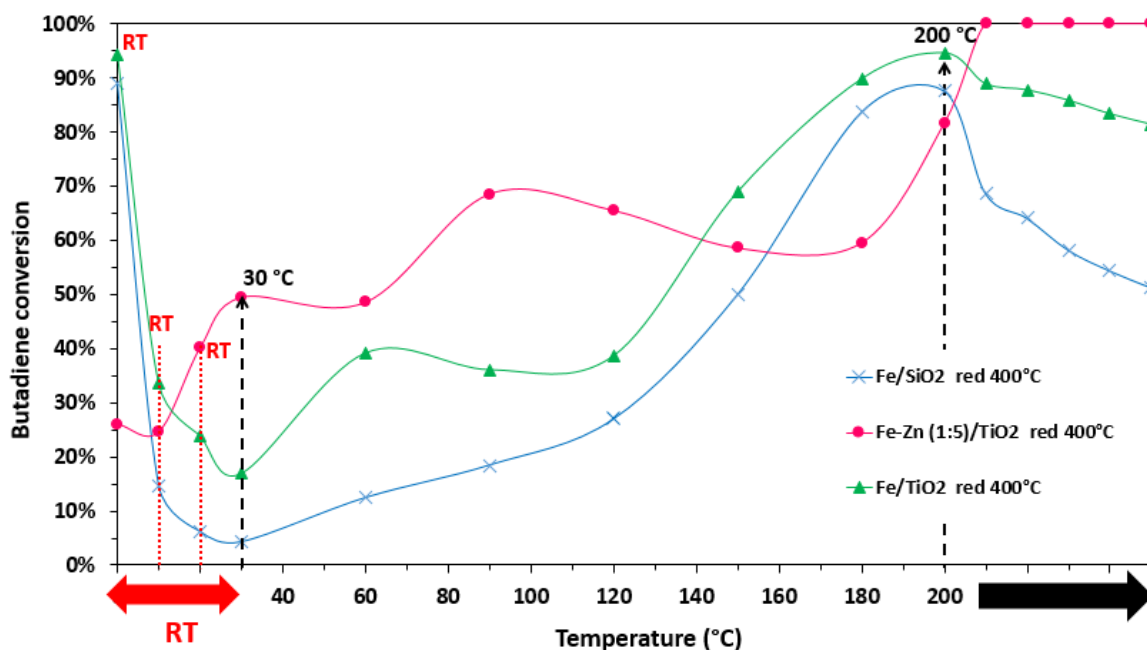
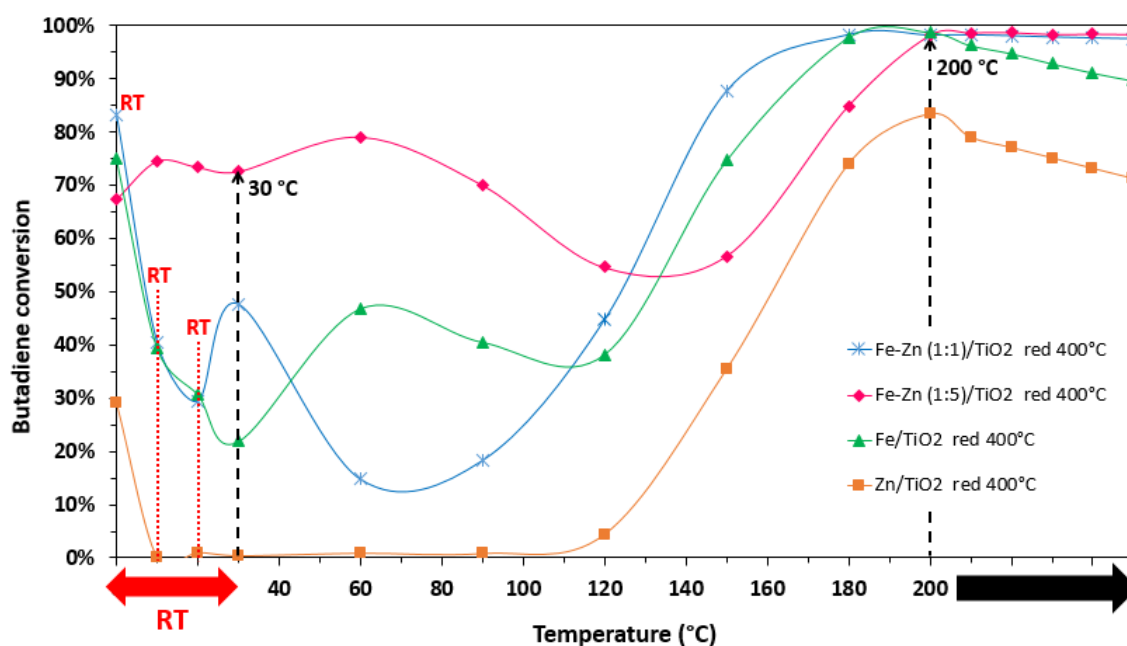**Figure 4.24.** Zoom in Figure 4.23 between 0-140 minutes. Representation of butadiene conversion over reaction temperature

Unfortunately, as a negative point, the bimetallic Fe-Zn 1:5/TiO$_2$ showed the poorest selectivity to alkenes, depicting some instabilities at the beginning and then achieving a moderate increase. In any case, the alkanes formation is still very low, especially in the case of the monometallic catalysts *(Figure 4.25)*.
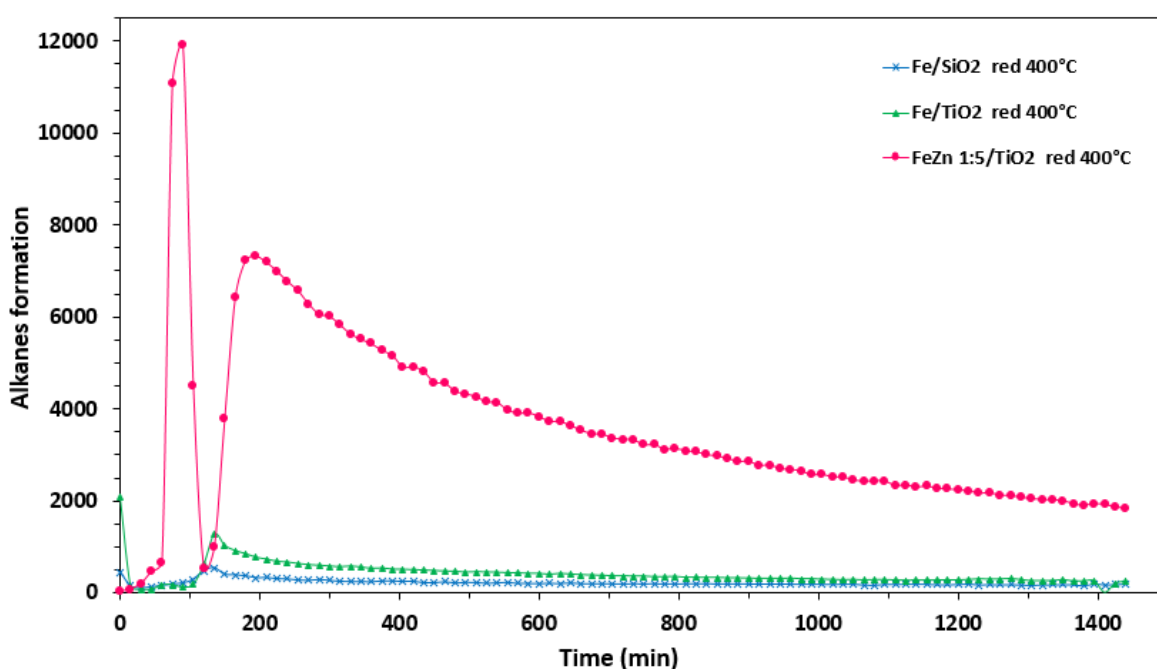
Figure 4.25. Alkanes formation as a function of the time over Fe/TiO$_2$ (green), Fe/SiO$_2$ (blue) and Fe-Zn 1:5/TiO$_2$ (pink). All samples synthesised by Chemical Reduction and previously reduced at 400 °C

> *Catalytic performance conclusions*

In first place, Fe/TiO$_2$ sample prepared by DPu and reduced at 400°C exhibited higher butadiene conversion than the same material reduced at 500°C despite the lower iron reduction extent estimated by TPR. This result also validates the choice of 400 °C as the maximum reduction temperature for bimetallic Fe-Zn samples, which permits to avoid the loss of Zn by evaporation at high temperature.

On the other hand, no very marked difference is appreciated between both synthesis methods applied in this study, but it is remarkable that samples prepared by Chemical Reduction show a slightly higher activity and stability. Moreover, the peculiar behaviour of bimetallic Fe-Zn 1:5/TiO$_2$ prepared by chemical reduction which presents an activation with time at RT is intriguing and may deserve additional investigations.

In addition, the highly loaded Zn/TiO$_2$ presented some significant activity at 200 °C in selective hydrogenation of 1,3-butadiene which was not expected. Thus, it is probably, at least partially, the reason why the activity of the bimetallic Fe-Zn 1:5/TiO$_2$ catalysts prepared by DPu and Chemical Reduction proved to be higher than the one of the monometallic Fe/TiO$_2$ samples, which could be interpreted as the addition of the respective activities of iron and zinc, at least at 200 °C. As it was already mentioned in the characterization section, TEM images revealed that iron and zinc are in close contact to each other although it was not possible to demonstrate by XRD the presence of any alloy formation. Finally, it worth to underline the high selectivity of most of the studied catalysts towards alkenes, with only limited alkanes formation.

CHAPTER 5   CONCLUSION AND FUTURE WORK

The present study investigates the applicability of supported monometallic Fe and Zn catalysts and bimetallic Fe-Zn catalysts in the selective hydrogenation of 1,3-butadiene. Therefore, the objective is to find a good catalyst in terms of activity, stability and selectivity. However, there are other important characteristics to take into account regarding the metallic active phase such as its abundancy, its price and its toxicity. This is the reason why iron is selected as an alternative to palladium whose properties have been already revealed successful in that reaction. Furthermore, it is well known that bimetallic materials present unique properties and, in particular, the promising effect of Zn addition on the catalytic performances of several transition metals has been reported.

Two preparation methods are also investigated. However, no important differences are evidenced in selective hydrogenation of butadiene, but the fact that the chemical reduction method leads to slightly higher activity and stability is promising as it is a rather simple method.

In addition, one of the most surprising findings is the noteworthy activity of the monometallic Zn/TiO_2 in this reaction. In fact, it is concluded that the best catalyst is the TiO_2 supported bimetallic Fe-Zn 1:5. At low reaction temperature, the active phase is mainly the iron one as the monometallic Zn/TiO_2 does not present any significant activity below 150 °C, but at 200 °C the activity of the bimetallic catalysts may correspond to the summation of the activities of the iron and zinc phases, at least partly.

Noting that Zn is a very cheap non-noble metal, it should be necessary to keep on searching its beneficial properties in selective hydrogenation 1,3-butadiene. Moreover, the question of the oxidation state of the Zn and Fe active species is still arising. As zinc oxide is hardly reducible up to 400 °C in the absence of another metal, the active zinc species in Zn/TiO_2 correspond probably to an oxidized form. Activation of H_2 by zinc oxide as well as selective hydrogenation of dienes was reported in the literature [42] and the use of Zn as an active phase for selective hydrogenation might be worth exploring.

Regarding iron, its activity at low temperature and high selectivity towards alkenes are very promising and the nature of the oxidation state of the active iron phase is also questionable as incomplete reduction of iron at 400 °C results in higher activity than full one at 500 °C. The use of X-Ray photoelectron spectroscopy (XPS) after *in situ* reduction of the samples may bring some important information on this aspect.

APPENDICES

CHARACTERIZATION TECHNIQUES

o   X-Ray Diffraction (XRD) analysis

XRD analysis is a non-destructive characterization tool used in materials science and solid state chemistry. Each crystalline material always gives the same characteristic X-ray powder pattern independently of the others in a mixture of substances, it is like a fingerprint used for its identification. Due to this property, XRD is mainly employed to determinate each compound in a sample and to characterize its structure. In a way that parameters such as phase identity, phase purity, lattice parameters, crystallinity, crystal structure and percent phase composition can be obtained from powder x-ray diffraction [43].

The operation procedure is based on sample scattering with a monochromatic beam of X-rays photons (one wavelength by a filter or a crystal monochromator). When an X-Ray beam hits an atom, the electrons around it start to oscillate with the same frequency as the incoming beam. In almost all directions it will be found destructive interference (out of phase). However, in a crystal, there will be constructive interference due to the regular pattern of their atoms so the waves will be in phase and X-Ray beams will leave the sample at various directions.

Noting that constructive interferences are produced when conditions satisfy Bragg's Law ($n\lambda = 2d\ sin\theta$) which states that when the radiation is incident onto a crystal surface, its angle of incidence, θ, will reflect back with a same angle of scattering. And, when the path difference, d, is equal to a whole number, n, of wavelength (remaining in phase), the scattered waves interfere constructively. Therefore, Bragg's Law relates the lattice spacing and diffraction angle which, in turn, is a function of X-ray intensity.

The X-Rays beam production consists of bombarding a metal (Cu and Mo usually) with a beam of high-speed electrons whose emission is produced from a hot filament (Tungsten is the most common material). When the beam impacts on the metal, electrons are ejected and drop from a lower level (1s) to an upper level (2p or 3p) filling the atom vacancies and giving rise to X-Rays emission [43].

o N_2-adsorption analysis. Brunauer–Emmett–Teller (BET)

BET analysis provides information on the sample specific surface area which is related to particle size, particle morphology, surface texturing and porosity [44]. This analysis technique is based on Brunauer–Emmett–Teller theory which explains physical adsorption of inert gas molecules (ex: Nitrogen) on a solid surface. Specific surface area of a material can be determined by calculating the amount of

adsorbate corresponding to a monolayer on the surface at a given pressure. It is derived from van der Waals forces that are established between the adsorbent surface area of sample and adsorbate gas molecules. Surface area is determined by monolayer formation and the principle of capillary condensation is applied to detect the presence of pores, pore size distribution and pore volume. So not only BET surface area can be accomplished by this technique but also other useful information. Besides, it is a cheap, fast and reliable technique. The basis of BET theory is an extension of Langmuir theory (monolayer adsorption) to multilayer adsorption on solid materials which is more realistic than the presupposition of monolayers. An adsorption isotherm is obtained by measuring the amount of gas adsorbed across a wide range of pressures at a fixed temperature (typically liquid N_2, 77 K) [45]. Conversely desorption isotherms are achieved by measuring gas removed as pressure is reduced. There are 6 types of isotherms but only Types II, IV and VI can be measured by BET since Types III and V present debilitated interactions between gas and adsorbent.

o Transmission Electron Microscopy (TEM)

Transmission electronic microscopy (TEM) is a significant analytical tool which procures crystallographic, morphologic and compositional information on materials. In this technique, a beam of electrons is transmitted through a sample causing the interaction between both and giving rise to an image which is magnified and focused onto an imaging instrument (a layer of photographic film or a fluorescent screen). The image resolution in TEM apparatus is very high due to the fact that the wavelength of electrons is dependent on the energy and, then, can be adjusted to achieve a smaller wavelength. Electrons can be engendered by field emission or by thermionic discharge and, next, they are speeded up by an electric field and focused on the specimen. Sample thickness must be sufficiently low to detect electrons.

REFERENCES

[1]   N. N. Lebedev, *Chemistry and technology of basic organic and petrochemical synthesis*, Imported P. 1984.

[2]   Z. Wang, G. Wang, C. Louis, and L. Delannoy, "Novel non-noble bimetallic Cu-Zn/TiO2catalysts for selective hydrogenation of butadiene," *J. Catal.*, vol. 347, pp. 185–196, 2017.

[3]   "Chapter 2 Catalytic processes in industry," 1999.

[4]   M. Eramo, "Global Ethylene Market Outlook: Low Cost Feedstocks Fuel The next Wave of Investments in North America and China."

[5]   A. Hugon, L. Delannoy, J.-M. Krafft, and C. Louis, "Selective Hydrogenation of 1 , 3-Butadiene in the Presence of an Excess of Alkenes over Supported Bimetallic Gold - Palladium Catalysts," *J. Phys. Chem. C*, vol. 4, no. i, pp. 10823–10835, 2010.

[6]   F. H. P. and K. D. Ruhnke, "Butene-1 containing feed purification process (CS-165)," 1981.

[7]   M.L.Derrien, *Studies in Surface Science and Catalysis, Chapter 18 Selective Hydrogenation Applied to the Refining of Petrochemical Raw Materials Produced by Steam Cracking*, Elsevier. 1986.

[8]   B. J. B. M. E. T. W. D. C. J. E. Bercaw, "Journal of the American Chemical Society," vol. 112, p. 1566, 1990.

[9]   A. Aguilar-Tapia, L. Delannoy, C. Louis, C. W. Han, V. Ortalan, and R. Zanella, "Selective hydrogenation of 1,3-butadiene over bimetallic Au-Ni/TiO2catalysts prepared by deposition-precipitation with urea," *J. Catal.*, vol. 344, no. 3, pp. 515–523, 2016.

[10]   Z. Wang, E. Doctorale, D. Physique, and P. Z. Wang, "Selective Hydrogenation of Butadiene over Non-noble Bimetallic Catalysts," UPMC, 2017.

[11]   N. L. M.Garcia-Mota, J.Gomez-Diaz, G.Novell-Leruth, C.Vargas-Fuentes, L.Bellarosa, B.Bridier, J.Perez-Ramirez, "Theoretical Chemistry Accounts 128," 2011, pp. 663–673.

[12]   Z. Wang, D. Brouri, S. Casale, L. Delannoy, and C. Louis, "Exploration of the preparation of Cu/TiO2catalysts by deposition-precipitation with urea for selective hydrogenation of unsaturated hydrocarbons," *J. Catal.*, vol. 340, pp. 95–106, 2016.

[13]   Z. Wang, G. Wang, C. Louis, and L. Delannoy, "Novel non-noble bimetallic Cu-Zn/TiO2catalysts for selective hydrogenation of butadiene," *J. Catal.*, vol. 347, pp. 185–196, 2017.

[14]   L. Piccolo and L. Kibis, "The partial hydrogenation of butadiene over Al13Fe4: A surface-science study of reaction and deactivation mechanisms," *J. Catal.*, vol. 332, pp. 112–118, 2015.

[15]   V. Kelsen, B. Wendt, S. Werkmeister, K. Junge, M. Beller, and B. Chaudret, "The use of ultrasmall iron(0) nanoparticles as catalysts for the selective hydrogenation of unsaturated C-

C bonds," *Chem. Commun.*, vol. 49, no. 33, pp. 3416–3418, 2013.

[16]   R. Hudson *et al.*, "Highly efficient iron(0) nanoparticle-catalyzed hydrogenation in water in flow," *Green Chem.*, vol. 15, no. 8, p. 2141, 2013.

[17]   W. J. Liu, T. T. Qian, and H. Jiang, "Bimetallic Fe nanoparticles: Recent advances in synthesis and application in catalytic elimination of environmental pollutants," *Chem. Eng. J.*, vol. 236, pp. 448–463, 2014.

[18]   G. Gómez, P. G. Belelli, G. F. Cabeza, and N. J. Castellani, "A theoretical view of 1,3-butadiene selective hydrogenation toward cis-2-butene on Pd-Ni layered catalyst," *Appl. Surf. Sci.*, vol. 353, pp. 820–828, 2015.

[19]   N. A. Khan, M. B. Zellner, L. E. Murillo, and J. G. Chen, "A comparison of similarities and differences in the activities of Pt / Ni (111) and Ni / Pt (111) surfaces," *Catal. Letters*, vol. 95, no. May, pp. 4–9, 2004.

[20]   N. J. K. Studt F., Abild-Pedersen F., Bligaard T., Sorensen R.Z., Christensen C.H., "Identification of Non-Precious Metal Alloy Catalysts for Selective Hydrogenation of Acetylene," *Science (80-.).*, vol. 320, p. 1320, 2008.

[21]   K. Bourikas, C. Kordulis, and A. Lycourghiotis, "Titanium dioxide (Anatase and Rutile): Surface chemistry, liquid-solid interface chemistry, and scientific synthesis of supported catalysts," *Chem. Rev.*, vol. 114, no. 19, pp. 9754–9823, 2014.

[22]   S. Derrouiche *et al.*, "Unusual behaviour of Au/ZnO catalysts in selective hydrogenation of butadiene due to the formation of a AuZn nanoalloy," *Catal. Sci. Technol.*, vol. 6, no. 18, pp. 6794–6805, 2016.

[23]   A. Hugon, L. Delannoy, and C. Louis, "Supported gold Catalysts for Selective Hydrogenation of Butadiene in the Presence of an excess of alkenes," *Gold Bull.*, vol. 41, no. 2, pp. 127–138, 2008.

[24]   P. Burattin, M. Che, and C. Louis, "Characterization of the Ni(II) Phase Formed on Silica Upon Deposition–Precipitation," *J. Phys. Chem. B*, vol. 101, no. 36, pp. 7060–7074, 1997.

[25]   V. K. Kaushik, C. Sivaraj, and P. K. Rao, "ESCA characterization of copper/alumina catalysts prepared by deposition - precipitation using urea hydrolysis," *Appl. Surf. Sci.*, vol. 51, no. 1–2, pp. 27–33, 1991.

[26]   G. V. Nano and T. J. Strathmann, "Ferrous iron sorption by hydrous metal oxides," *J. Colloid Interface Sci.*, vol. 297, no. 2, pp. 443–454, 2006.

[27]   T. Hiemstra and W. H. van Riemsdijk, "Adsorption and surface oxidation of Fe(II) on metal (hydr)oxides," *Geochim. Cosmochim. Acta*, vol. 71, no. 24, pp. 5913–5933, 2007.

[28]   M. Stefaniuk, P. Oleszczuk, and Y. S. Ok, "Review on nano zerovalent iron (nZVI): From synthesis to environmental applications," *Chem. Eng. J.*, vol. 287, pp. 618–632, 2016.

[29]   A. Liu, J. Liu, and W. xian Zhang, "Transformation and composition evolution of nanoscale zero valent iron (nZVI) synthesized by borohydride reduction in static water," *Chemosphere*, vol. 119, pp. 1068–1074, 2015.

[30]   K. Xu *et al.*, "Nanocrystalline iron-boron catalysts for low-temperature CO hydrogenation: Selective liquid fuel production and structure-activity correlation," *J. Catal.*, vol. 339, pp. 102–110, 2016.

[31]   A. Liu, J. Liu, J. Han, and W. X. Zhang, "Evolution of nanoscale zero-valent iron (nZVI) in water: Microscopic and spectroscopic evidence on the formation of nano- and micro-structured iron oxides," *J. Hazard. Mater.*, vol. 322, pp. 129–135, 2017.

[32]   J. W. Geus and A. J. van Dillen, "Preparation of Supported Catalysts by Deposition–Precipitation," in *Handbook of Heterogeneous Catalysis*, 2008, pp. 428–467.

[33]   J. Bjerrum, "Stability constants of metal-ion complexes," *Chem. Soc.*, 1964.

[34]   W. H. R. Shaw and J. J. Bordeaux, "The Decomposition of Urea in Aqueous Media," *J. Am. Chem. Soc.*, vol. 77, no. 18, pp. 4729–4733, 1955.

[35]   W. P. Hsieh, J. R. Pan, C. Huang, Y. C. Su, and Y. J. Juang, "Enhance the photocatalytic activity for the degradation of organic contaminants in water by incorporating TiO2 with zero-valent iron," *Sci. Total Environ.*, vol. 408, no. 3, pp. 672–679, 2010.

[36]   Y. Li, T. Li, and Z. Jin, "Stabilization of Fe 0 nanoparticles with silica fume for enhanced transport and remediation of hexavalent chromium in water and soil," *J. Environ. Sci.*, vol. 23, no. 7, pp. 1211–1218, 2011.

[37]   A. Hugon, L. Delannoy, and C. Louis, "Influence of the reactant concentration in selective hydrogenation of 1,3-butadiene over supported gold catalysts under alkene rich conditions: A consideration of reaction mechanism," *Gold Bull.*, vol. 42, no. 4, pp. 310–320, 2009.

[38]   R. . S. H. Glocker, "S c h r e d b e r $1.," pp. 1089–1102, 1924.

[39]   T. Imoto, Y. Harano, Y. Nishi, and S. Masuda, "The Reduction of Zinc Oxide by Hydrogen. III. The Effect of Nitrogen on the Reduction," *Bull. Chem. Soc. Jpn.*, vol. 37, no. 4, pp. 441–444, 1964.

[40]   S. Lew, "the Reduction of Zinc Titanate Solids and Zinc," *Chem. Eng. Sci.*, vol. 47, no. 6, pp. 1421–1431, 1992.

[41]   J. Zieliński, I. Zglinicka, L. Znak, and Z. Kaszkur, "Reduction of Fe2O3 with hydrogen," *Appl. Catal. A Gen.*, vol. 381, no. 1–2, pp. 191–196, 2010.

[42]   W. C. Conner and R. J. Kokes, "Hydrogen activation on Zinc Oxide," vol. 210, pp. 199–210, 1975.

[43]   R. S. Devoto, "Transport properties of ionized monoatomic gases," *Phys. fluids*, vol. 9, p. 1230, 1966.

[44]   a Trunschke, "Surface area and pore size determination," *Mod. Methods Heterog. Catal. Res.*, vol. 1, no. November, 2013.

[45]   N. Leddy, "SURFACE AREA AND Adsorption," *C. Anal.*, vol. 5, pp. 23–64, 2012.